An assessment of basal melt parameterisations for Antarctic ice shelves

Clara Burgard[1], Nicolas C. Jourdain[1], Ronja Reese[2], Adrian Jenkins[2], and Pierre Mathiot[1]

[1]Univ. Grenoble Alpes, CNRS, IRD, Grenoble INP, IGE, 38000 Grenoble, France
[2]Department of Geography and Environmental Sciences, Northumbria University, Newcastle Upon Tyne, UK

Correspondence: C. Burgard (clara.burgard@univ-grenoble-alpes.fr)

Abstract. Ocean-induced ice-shelf melt is the highest uncertainty factor in the Antarctic contribution to future sea level. Several parameterisations exist to link oceanic properties to basal melt and force ice-sheet models. Here, we assess the potential of a range of existing basal melt parameterisations to emulate basal melt rates simulated by a cavity-resolving ocean model on the circum-Antarctic scale. To do so, we re-tune the parameterisations in a perfect model approach, and compare the melt rates produced by the newly tuned parameterisations to the melt rates simulated by the ocean model. We find that the quadratic dependence of melt to thermal forcing without dependency on the individual ice-shelf slope and the plume parameterisation yield the best compromise, in terms of integrated shelf melt and spatial patterns. The box, PICOP parameterisation and quadratic parameterisations with slope dependency yield basal melt rates further from the model reference. The linear parameterisation cannot be recommended as the resulting integrated ice-shelf melt is comparably furthest from the reference. When using offshore hydrographic input fields in comparison to properties on the continental shelf, all parameterisations perform worse, however the box and the slope-dependent quadratic parameterisations yield the comparably best results. Additionally to the new tuning, we provide uncertainty estimates for the tuned parameters.

1 Introduction

The Antarctic ice sheet has been losing mass at a rapid pace in past decades, increasing the Antarctic contribution to sea-level rise from 0.14 ± 0.02 mm yr^{-1} between 1992 and 2001 to 0.55 ± 0.07 mm yr^{-1} between 2012 and 2016 (Oppenheimer et al., 2019). Most of this mass loss has been attributed to an acceleration in ice flow across the grounding line, i.e. from the grounded part to the floating ice shelves at the outskirts of the ice sheet (e.g. Mouginot et al., 2014; Rignot et al., 2014; Scheuchl et al., 2016; Khazendar et al., 2016; Shen et al., 2018; The IMBIE Team, 2018).

Ice shelves themselves can moderate the pace of the mass loss. Being several hundreds of meters thick and interacting with land or shallow rocks, they act as natural barriers to restrain the grounded ice-sheet flow into the ocean. Ice shelves have been thinning all around Antarctica in past decades (Rignot et al., 2013; Paolo et al., 2015; Adusumilli et al., 2020), driven by an increasing amount of warm circumpolar deep water (CDW) intruding on to the continental shelf and into the cavities below the ice shelves (Jacobs et al., 2011; Wouters et al., 2015; Khazendar et al., 2016; Jenkins et al., 2018). Thinning reduces the ice shelves' buttressing potential, which means that the restraining force that they exert on the ice outflow at the grounding line is

25 lower and more ice is discharged into the ocean. In some bedrock configurations, increased melt can trigger marine ice sheet
    instabilities (e.g. Weertman, 1974; Schoof, 2007; Gudmundsson et al., 2012). This is why ocean-induced sub-shelf melt, which
    we call *basal melt* in the following, is a crucial component for simulations of the Antarctic contribution to future sea-level
    evolution. Still, it is currently the main uncertainty source in such projections (e.g. Edwards and the ISMIP6 Team, 2021; Hill
    et al., 2021).

30 Basal melt is a result of positive thermal forcing, i.e. water above the local freezing point getting in contact with the lower
    side of the ice shelf. To represent basal melting accurately in models, we therefore need to accurately simulate the hydro-
    graphic properties of the water entering the ice-shelf cavity and to resolve the circulation of the water masses within the cavity.
    Ideally, this would be done in a coupled ocean–ice-sheet simulation resolving the ocean circulation in the cavity below the ice
    shelf (e.g. De Rydt and Gudmundsson, 2016; Seroussi et al., 2017). However, running such simulations on a circum-Antarctic
35 scale is computationally expensive and this approach is therefore currently not suitable for large ensembles or multi-centennial
    time scales. Furthermore, most global climate models, such as the ones used in the most recent phases of the Coupled Model
    Intercomparison Project (CMIP, Taylor et al., 2012; Eyring et al., 2016), still poorly represent the ocean dynamics along the
    Antarctic margins and do not resolve ice-shelf cavities (Beadling et al., 2020; Heuzé, 2021). As a consequence, the Antarc-
    tic contribution to sea-level rise is often computed by standalone ice-sheet models or ice-sheet models coupled to a coarse-
40 resolution ocean model, which can be called "coupling of intermediate complexity" (Kreuzer et al., 2021). In both cases, basal
    melting is parameterised based on ocean properties simulated by the ocean model for the region in front of the ice shelf (e.g.
    Jourdain et al., 2020; Reese et al., 2020).

    On the one hand, ice-sheet models need information about the spatial distribution of melt below the ice shelf. On the other
    hand, non-cavity-resolving ocean models only provide the hydrographic properties in front of the ice shelf ("far field" in the
45 following). Several parameterisations of varying complexity have been developed in the last 20 years to derive melt rates from
    far-field ocean properties on the circum-Antarctic scales (Beckmann and Goosse, 2003; Holland et al., 2008; DeConto and
    Pollard, 2016; Reese et al., 2018; Lazeroms et al., 2018, 2019; Favier et al., 2019; Jourdain et al., 2020). However, assumptions
    in the various formulations differ, giving rise to a large variety of melt patterns (Favier et al., 2019). As observations of the
    hydrographic properties in front of ice shelves are sparse, it is challenging to evaluate the performance and uncertainty of
50 the different basal melt parameterisations and therefore make a recommendation on which one to incorporate in standalone
    ice-sheet models or ocean–ice-sheet couplings of intermediate complexity.

    Favier et al. (2019) evaluated various melt parameterisations through a comparison between standalone ice-sheet simulations
    with parameterised melt and a small ensemble of coupled ice-sheet–ocean simulations (resolving the ocean circulation and melt
    beneath the ice shelf). This work was based on an idealised modelling setup consisting of an evolving but relatively small cavity,
55 with idealised cooling and warming transitions similar to the MISMIP+ and MISOMIP framework (Asay-Davis et al., 2016).
    Their parameterisation ranking was then used as a basis to choose the standard melt parameterisation of ISMIP6 (Jourdain
    et al., 2020; Nowicki et al., 2020). However, when these recommendations were applied to ice-sheet models with realistic and
    diverse ice-shelf geometries, substantial empirical temperature corrections had to be applied to reproduce observational melt
    rates in the various sectors of Antarctica, and the pattern and sensitivity to ocean warming were still questionable (Jourdain

60 et al., 2020; Reese et al., 2020). Previous studies also had to apply sector-dependent corrections or calibrations (Lazeroms et al., 2018; DeConto and Pollard, 2016).

In this study, we assess the potential of the diverse parameterisations to represent melt rates without basin- or ice-shelf-dependent temperature correction or calibration. To do so, we explore their ability to emulate an ensemble of circum-Antarctic ice-shelf-resolving ocean simulations representing a total of 127 years of basal melt rates responding to a variety of ocean

65 conditions. This assessment is particularly relevant for the application of the parameterisations in pan-Antarctic ice-sheet simulations. In a first step, we describe the ensemble of ocean simulations that we use as our "virtual" reality, the data, and the different parameterisations we assess. We also revisit the formulation of several simple parameterisations to emphasize the physical hypotheses behind them. In a second step, we tune the parameterisations using the ocean simulation as a reference to assess how close they can be to the reference and make them comparable between each other. In a third step, we compare

70 the resulting melt rates with the melt rates simulated by the ocean model and we provide recommendations for applications in pan-Antarctic ice-sheet simulations.

2   Evaluation framework

We use a perfect-model approach to assess and re-tune different basal melt parameterisations proposed by previous literature, from very simple to more complex ones. This means that we use the ocean state and melt rates simulated by a cavity-resolving

75 ocean model as a "virtual" reality. There are several advantages to this method: (1) we have a larger amount of data, both over time and space, than we have from observations, and (2) this approach provides a self-consistent framework where the link between ocean properties in front of the ice shelf, which we feed into the different parameterisations, and the resulting melt rates at the ice-ocean interface is physically sound in time and space. In the following we present the ocean model and its configuration, the basal melt parameterisations, and the tuning method.

80 ### 2.1   The ocean model NEMO

2.1.1   Basic model setup

Our study is based on simulations conducted with the version 4.0.4 of the 3-D primitive-equation coupled ocean–sea-ice model NEMO (Nucleus for European Modelling of the Ocean, NEMO Team, 2019). It is run in a global configuration referred to as eORCA025 (Storkey et al., 2018), which is a grid of $0.25°$ resolution in longitude, i.e. a resolution of 8 km in both directions

85 at $70°$S, which is sufficient to capture the basic ocean circulation below multiple Antarctic ice shelves (Mathiot et al., 2017; Bull et al., 2021). The nonlinear free surface is defined through the time varying $z^{\star}$ vertical coordinate (Adcroft and Campin, 2004). A new vertical grid was developed, with 121 vertical levels (vs 75 commonly used) and a depth-dependent resolution of 1 m in the surface layers, 20 m between 100 m and 1000 m depth and 200 m at 6000 m depth. As most ice shelves have their grounding lines above or near 1000 m depth and their front below 100 m, this enables a quasi uniform vertical resolution

90 across the Antarctic ice shelves.

In this version of NEMO, the SI3 model represents sea-ice dynamics, thermodynamics, brine inclusions and subgrid-scale sea-ice thickness variations (NEMO Sea Ice Working Group, 2019). Also, we use the Lagrangian iceberg model developed by Marsh et al. (2015) and improved by Merino et al. (2016) to account for sub-surface currents and temperatures. The Antarctic calving fluxes are constant and based on the satellite estimates by Rignot et al. (2013). The observed fluxes are imposed at the front of individual ice shelves with a uniform random distribution for all grid cells of a given ice shelf front.

The basal melt of ice shelves is represented by the three equations as described in Asay-Davis et al. (2016) implemented into NEMO by Mathiot et al. (2017):

1. the heat balance at the ice-ocean interface:

$$c_{\mathrm{oc}}\rho_{\mathrm{oc}}\gamma_T(T_{\mathrm{oc}} - T_f) = -L_i f_w - \rho_i c_i \kappa \frac{T_a - T_{\mathrm{oc}}}{h_{\mathrm{isf}}} \tag{1}$$

2. the salt balance at the ice-ocean interface:

$$\rho_{\mathrm{oc}}\gamma_S(S_{\mathrm{oc}} - S_b) = -S_b f_w \tag{2}$$

3. the pressure and salinity-dependent freezing temperature:

$$T_f = \lambda_1 S_b + \lambda_2 + \lambda_3 z_{\mathrm{isf}} \tag{3}$$

where c_{oc} and c_i are, respectively, the specific heat capacity of the seawater and the ice, ρ_{oc} and ρ_i are, respectively, the density of the seawater and the ice, T_{oc} and S_{oc} are the temperature and salinity averaged over a boundary layer below the ice shelf, T_f is the freezing point, L_i is the latent heat of fusion, f_w is the meltwater mass flux, κ is the thermal diffusivity of ice, T_a is the atmospheric surface temperature, here assumed constant at -20°C, h_{isf} is the ice shelf thickness, S_b is the salinity at the ice-ocean interface, λ_1, λ_2 and λ_3 are the coefficients for the freezing point equation (close to the ones listed in Table 2), z_{isf} is the depth of the ice-shelf draft, and γ_T and γ_S are the exchange velocities for temperature and salt:

$$\gamma_T = C_d^{1/2}\Gamma_T\sqrt{u_{\mathrm{oc}}^2 + u_{\mathrm{tide}}^2} \tag{4}$$

$$\gamma_S = C_d^{1/2}\Gamma_S\sqrt{u_{\mathrm{oc}}^2 + u_{\mathrm{tide}}^2} \tag{5}$$

where u_{oc} is the ocean model velocity in the top boundary layer, u_{tide} is the tidal velocity, C_d is the drag coefficient, set to 2.5×10^{-3}, and Γ_T and Γ_S are the heat and salt exchange coefficients and are set respectively to 0.014 and 4×10^{-4} as in Hausmann et al. (2020) and Bull et al. (2021). The top boundary-layer thickness is set to 30 m.

In contrast to Mathiot et al. (2017), we prescribe a constant but spatially varying tidal velocity u_{tide} in Eq. (4) and Eq. (5) at the upper interface (ice shelf/ocean). Following the recommendations of Jourdain et al. (2019), it is calculated as 0.656 times the mean barotropic tidal velocity derived from constituents M2, S2, N2, K1, Q1 and O1 of the CATS 2008 model (Padman

et al., 2008; Howard et al., 2019) using Eq. (7) of Jourdain et al. (2019). While the conclusions of Jourdain et al. (2019) were
120   limited to the Amundsen Sea sector, more recent work gives confidence that this method to represent tide-induced melt is
relevant at the circum-Antarctic scale (Hausmann et al., 2020; Huot et al., 2021; Richter et al., 2020).

The model bathymetry is derived from ETOPO1 in the open ocean (Amante and Eakins, 2009), GEBCO (IHO and BODC
IOC, 2003) on the continental shelves (excluding Antarctic continental shelf). The Antarctic continental shelf bathymetry and
ice shelf draft are based on Bedmachine Antarctica version 2 (Morlighem, 2020; Morlighem et al., 2020). The simulations
125   are forced with the climatological geothermal heat flux from Goutorbe et al. (2011), and atmospheric forcing from JRA55-do
version 1.4 (Tsujino et al., 2018). The turbulent and momentum fluxes are computed using the NCAR bulk formulae algorithm
(Large and Yeager, 2009). The ocean initial conditions are based on the WOA2018 climatological temperature and salinity
over 1981-2010 (Locarnini et al., 2018; Zweng et al., 2018; Garcia et al., 2019). The sea-ice initial conditions are taken from a
1980-2004 model climatology based on an upgrade of eORCA025 GO6 simulations (Storkey et al., 2018). Initial sea-ice and
130   ocean velocities are set to 0.

More details on the parameterisations common to all our simulations are presented in Appendix A.

2.1.2   Ensemble of simulations

We use an ensemble of four NEMO simulations that are based on different values of a small number of parameters. This is
an ensemble of opportunity, i.e. not specifically designed for this study, but it covers large ocean temperature variations, with
135   differences of up to $\pm 2°C$ in front of some ice shelves (Fig. 1), which is an amplitude comparable to typical RCP8.5 changes
during the 21st century (Barthel et al., 2020). Also, the different simulations cover several decades, and therefore include
interannual variability, which can affect basal melt rates (Hoffman et al., 2019).

The differences between the four simulations of the ensemble are listed in Table 1. None of the changed parameters has a
significant impact on the physics of ocean—ice-shelf interactions, and they mostly change the ocean properties further away
140   from the cavities. For example, for all simulations except HIGHGETZ, we assigned a land barrier along the 350 m isobath of
Bear Ridge East Flank in the Amundsen Sea to mimic the sea-ice blocking induced by grounded icebergs in that region, like
in Bett et al. (2020) and Nakayama et al. (2014).

The only difference affecting ocean–ice-shelf interactions is the ice-shelf topography of Getz. The total basal mass loss of
Getz in the HIGHGETZ simulation reaches $500 \, \text{Gt} \, \text{yr}^{-1}$ due to an underestimated thermocline depth that allows circumpolar
145   deep water to reach most of the ice shelf draft. This is a long-standing bias in our NEMO simulations (Mathiot et al., 2017;
Jourdain et al., 2017). As a consequence, the Getz ice shelf was artificially thinned by ~ 200 m in all other simulations of our
ensemble. This correction reduces the basal mass loss to $\sim 170 \, \text{Gt} \, \text{yr}^{-1}$, closer to observational estimates (Rignot et al., 2013;
Adusumilli et al., 2020).

As suggested by the simulation names, REALISTIC is the simulation closest to realistic conditions, COLDAMU remains
150   relatively cold in the Amundsen Sea, and WARMROSS triggers a warm state over the East Ross Shelf and much fresher high
salinity shelf water (HSSW). More details, including an evaluation of the REALISTIC simulation compared to observations,
are provided in Appendix B.
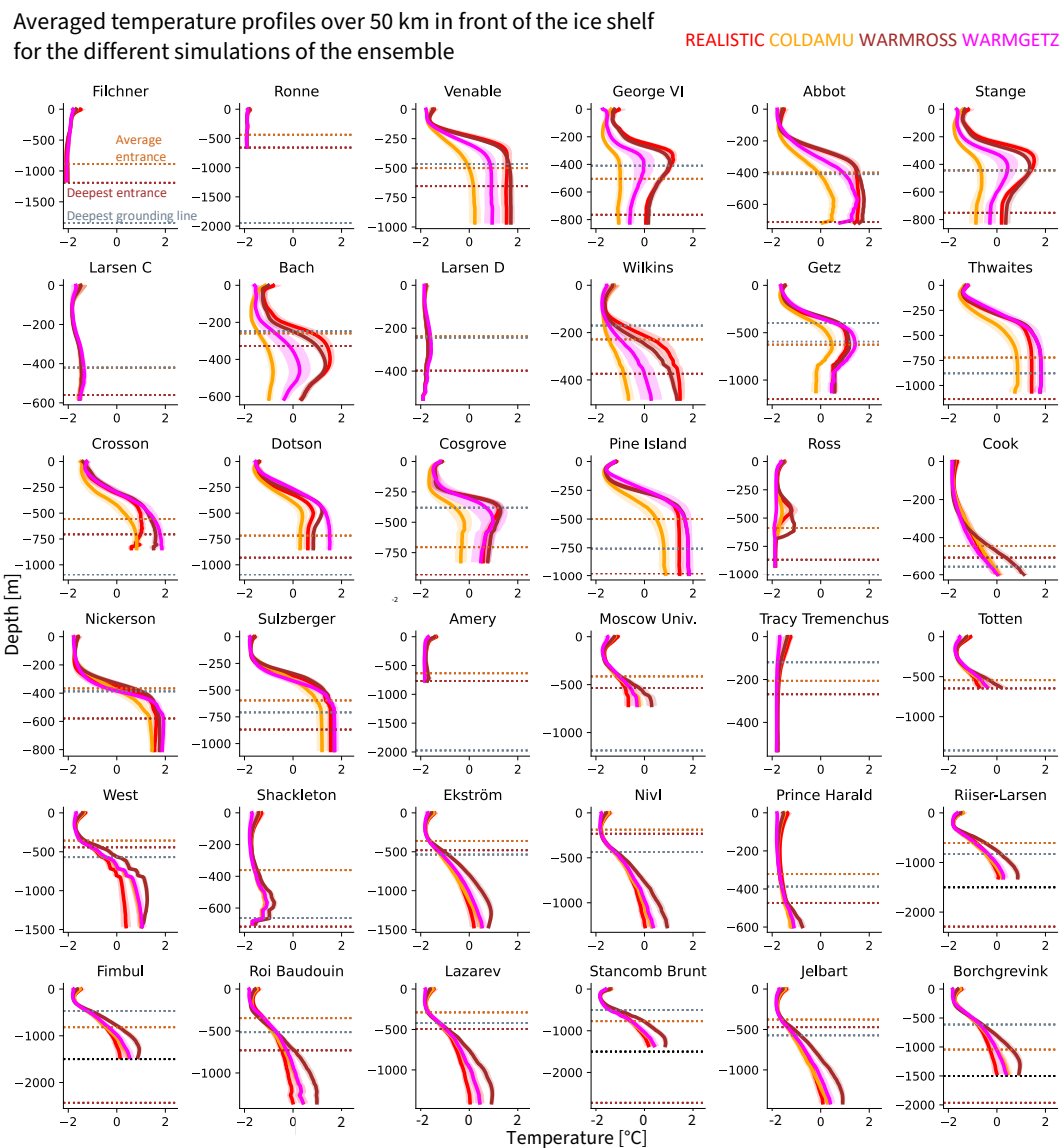
Figure 1. Comparison of mean input temperature profiles between the four different simulations (REALISTIC, COLDAMU, WARMROSS, WARMGETZ), averaged over 50 km on the continental shelf in front of the ice shelf. The shading represents the interannual variability (one standard deviation over time). The horizontal dotted lines show the average depth of the bed at the ice front (light brown), the largest depth of the bed at the ice front (dark brown) and the largest depth of the grounding line (grey). The deepest grounding line point for Getz ice shelf is different in the HIGHGETZ compared to the other simulations due to the artificial thinning in the latter (see Sec. 2.1.2).

For this study, we interpolate the NEMO output bilinearly to a stereographic grid of 5 km spacing as all parameterisations are coded for stereographic grids which are commonly used for ice sheet models. In a second step, we cut out the different ice

Table 1. Description of the differences between the four simulations used. The AABW (AntArctic Bottom Water) restoring is described in Dufour et al. (2012). GM mixing is a parameterisation of adiabatic eddy mixing (Gent and McWilliams, 1990) used where local resolution is coarser than half the local Rossby radius. S2016 and M2015 are the iceberg size distribution provided by Stern et al. (2016) and Marsh et al. (2015), respectively. The land barrier at Bear Ridge mimics the sea-ice blocking induced by grounded icebergs in that region. Ice set 1 and Ice set 2 make use of different sea ice parameters. In Ice-set 2 (compared to Ice-set 1), the adaptative EVP rheology is turned off, the ice–ocean drag coefficient is set to 0.005 instead of 0.012, the snow conductivity changed from 0.31 to 0.35 W/m/K, and the frazil ice formation scheme is turned off. "Bug 2626" stands for a bug on the distribution of solar and non-solar radiation originally present in NEMO-v4.0.4 and corrected since then.

Simulation	Simulation period (Analysis period)	Isopycnal diffusion [m²/s]	Eddy-induced velocity coefficient [m²/s]	GM mixing	AABW restoring	Iceberg distribution	Barrier Bear Ridge	Sea ice parameters	Bug 2626	Getz geometry
REALISTIC	1979-2018 (1989-2018)	150	150	Yes	No	S2016	Yes	Ice set 2	No	Shallow
COLDAMU	1959-2008 (1980-2008)	150	n/a	No	No	M2015	Yes	Ice set 1	No	Shallow
WARMROSS	1959-2008 (1980-2008)	300	300	Yes	Yes	M2015	Yes	Ice set 1	No	Shallow
HIGHGETZ	1959-2018 (1980-2018)	150	n/a	No	No	M2015	No	Ice set 1	Yes	Realistic

155   shelves according to longitude and latitude boundaries (details found in Burgard (2021)). In a third step, we only keep the ice shelves with an area larger than 2500 km², as the circulation might not be resolved well enough by NEMO in smaller cavities (i.e. assuming an effective model resolution of $\sim 5\Delta x$). This results into the 36 resolved ice shelves shown e.g. in Fig. 1.

2.2   Basal melt parameterisations

We make the choice to assess parameterisations which have been developed for and applied on the circum-Antarctic scale.
160   These are the simple linear (Beckmann and Goosse, 2003) and quadratic (DeConto and Pollard, 2016; Holland et al., 2008; Favier et al., 2019; Jourdain et al., 2020) parameterisations, the plume parameterisation (Lazeroms et al., 2018, 2019), the box parameterisation (Reese et al., 2018) and the PICOP parameterisation (Pelle et al., 2019). There are also other parameterisations, but these have been only applied to single ice shelves. For example, Hoffman et al. (2019) propose a parameterisation combining an approximate solution of the plume equations to infer the temperature with the local/non-local formulation from
165   Favier et al. (2019) and apply it to investigate variability in the melt of Thwaites ice shelf.

In all the parameterisations, the main driver of basal melt is the thermal forcing. However, the various parameterisations differ in their definitions of the far-field temperature and salinity, in the link between these and the thermal forcing at the

ice-ocean interface, and in the complexity of the physical relationship between the thermal forcing and the melt rate. In the following, we present the different parameterisations. All implementations were done in Python (see Burgard, 2021), mainly

170 with the numpy (Harris et al., 2020), xarray (Hoyer and Hamman, 2017) and dask (Dask Development Team, 2016) packages.

2.2.1 Simple parameterisations

Over the past decades, several simple parameterisations of the link between the ocean properties in front of the ice shelf and the melt at the base of ice shelves have been proposed. In these simple parameterisations, the water temperature and salinity at a given point of the ice-shelf draft are extrapolated from the same depth from the mean profiles in front of the ice shelf, which

175 we call "far-field" temperature and salinity in the following. If the ice-shelf draft is shallower than the deepest entrance point, i.e. the deepest point of the bed at the ice-shelf front, we extrapolate to the depth of the deepest entrance point instead of the ice-draft depth. This extrapolation means that the thermal forcing is directly linked to the ocean properties in front of the shelf and the redistribution and transformation of water masses within the cavity is not accounted for in most of them. While some earlier simple parameterisations were based on sea-floor or vertically integrated ocean properties, recent results point to the

180 importance of the thermocline depth for melt rates (e.g. De Rydt et al., 2014; Favier et al., 2019). This is why we account for vertical profiles of the input properties in the following.

Several slightly different versions of the simple parameterisations have been formulated in past decades. To enable a consistent assessment and comparison, we start by revisiting these formulations in a common formalism.

Locally, the melt rate m (in meters of ice per second) is determined by the heat flux across the turbulent boundary layer

185 created by current shear against the ice base, and was formulated as follows in Jenkins et al. (2018) based on a linearisation of the three equations (Jenkins et al., 2010):

$$m = \frac{\rho_{\text{oc}}}{\rho_{\text{i}}} \left\{ \frac{C_d^{1/2} \Gamma_{TS}}{[L_i - c_i(T_i - T_{\text{f}})]/c_{\text{oc}}} \right\} U(T_{\text{oc}} - T_{\text{f}}) \tag{6}$$

where ρ_{oc} and ρ_{i} are, respectively, the density of seawater and ice, C_d is the ice–ocean drag coefficient, Γ_{TS} is a transfer coefficient combining information about heat and salt transfer, L_i is the latent heat of fusion, T_i, T_{oc}, and T_{f} are, respectively,

190 the temperature of the ice, the seawater temperature (far-field temperature at the depth of the ice draft), and the freezing point at the depth of the ice shelf base, and U is the current speed below the ice shelf.

Given that ice temperature has a relatively small effect on melt rates (Dinniman et al., 2016; Arzeno et al., 2014), we can rewrite Eq. (6), resulting in a melt rate:

$$m = \frac{c_{\text{oc}}}{L_i} \frac{\rho_{\text{oc}}}{\rho_{\text{i}}} \gamma_{TS}(T_{\text{oc}} - T_f) \tag{7}$$

195 with the turbulent exchange velocity:

$$\gamma_{TS} = C_d^{1/2} \Gamma_{TS} U \tag{8}$$

The simplest way to estimate melt rates from Eq. (7) is to assume a constant and uniform characteristic velocity (U_{Ant}) over all ice shelves, so that γ_{TS} is a constant parameter that can be tuned to match observations or simulations:

$$\gamma_{TS,\text{loc, Ant}} = C_d^{1/2}\Gamma_{TS}U_{\mathrm{Ant}} \tag{9}$$

200 The resulting parameterisation, referred to as the *linear-local* parameterisation, was initially proposed by Beckmann and Goosse (2003) and has been used in numerous ice-sheet simulations since then (e.g. Martin et al., 2011; Álvarez-Solas et al., 2011).

However, assuming a constant U_{Ant} over all Antarctica is not necessarily reasonable as velocities vary a lot within an ice-shelf cavity and from an ice shelf to another (Jourdain et al., 2017). Since the introduction of the *linear-local* parameterisation,
205 efforts have been made to include more information that could mimic the effect of the local geometry and of the vertical overturning circulation in the cavity on the melt rate. Jenkins et al. (2018), for example, propose to describe U with other variables and parameters. This formulation assumes that the ocean circulation along the ice draft is mostly governed by the geostrophic balance:

$$U = \frac{g}{-2\,|\,f\,|}\sin\theta\Delta\widetilde{\rho} \tag{10}$$

210 where g is gravity, f is the Coriolis parameter, θ is the slope of the ice shelf base relative to the horizontal, and $\Delta\widetilde{\rho}$ the dimensionless density deficit in the top boundary layer:

$$\Delta\widetilde{\rho} = P_0(\epsilon - 1)\,|\,T_{\mathrm{oc}} - T_{\mathrm{f}}\,| \tag{11}$$

where the subscript *oc* denotes the far-field temperature and salinity that is advected into the cavity, ϵ can be related to the relative efficiency of mixing across the thermocline that separates the boundary current from the warmer water below and
215 across the ice-ocean boundary layer, and P_0 is a constant defined as follows (Jenkins et al., 2018):

$$P_0 = \frac{\beta_S S_{\mathrm{oc}} - \beta_T[(T_{\mathrm{oc}} - T_{\mathrm{f}}) + (L_i - c_i(T_i - T_{\mathrm{f}}))/c_{\mathrm{oc}}]}{(T_{\mathrm{oc}} - T_{\mathrm{f}}) + (L_i - c_i(T_i - T_{\mathrm{f}}))/c_{\mathrm{oc}} - \lambda_1 S_{\mathrm{oc}}} \tag{12}$$

where β_S and β_T are the salt contraction and heat expansion coefficients respectively, and λ_1 is the liquidus slope (see Table 2).

Combining Eq. (6), Eq. (10), and Eq. (11), this results in the following formulation for the melt rate:

220 $$m = M_0\frac{g}{2\,|\,f\,|}\sin\theta P_0\epsilon(1 - \epsilon)\,|\,T_{\mathrm{oc}} - T_{\mathrm{f}}\,|\,(T_{\mathrm{oc}} - T_{\mathrm{f}}) \tag{13}$$

where M_0 is the term in braces in Eq. (6), which can be simplified, like in Eq. (7), to: $M_0 \approx C_d^{1/2}\Gamma_{TS}\frac{\rho_{\mathrm{oc}}}{\rho_{\mathrm{i}}}\frac{c_{\mathrm{oc}}}{L_i}$. Note that we use the absolute value of the thermal forcing in the term describing U because we consider the current speed, which has to be positive.

After a scale analysis based on the values in Table 2, a reasonable approximation of P_0 is: $P_0 \approx \frac{c_{\mathrm{oc}}}{L_i}\beta_S S_{\mathrm{oc}}$, which yields the
225 following formulation for the melt rate:

$$m = C_d^{1/2}\Gamma_{TS}\frac{\rho_{\mathrm{oc}}}{\rho_{\mathrm{i}}}\left(\frac{c_{\mathrm{oc}}}{L_i}\right)^2\beta_S S_{\mathrm{oc}}\frac{g}{2\,|\,f\,|}\sin\theta\epsilon(1 - \epsilon)\,|\,T_{\mathrm{oc}} - T_{\mathrm{f}}\,|\,(T_{\mathrm{oc}} - T_{\mathrm{f}}) \tag{14}$$

Table 2. Constant parameters used in the melt parameterisations. Note that, due to different reference densities, β_T and β_S differ between the box and plume parameterisation.

Symbol	Parameter	Value
General		
ρ_i	Ice density	917 kg m^{-3}
ρ_{oc}	Seawater density	1028 kg m^{-3}
g	Gravitational acceleration	9.81 m s^{-2}
f	Coriolis parameter	-1.4 $\times$ 10^{-4} s^{-1}
L_i	Latent heat of fusion	3.34 $\times$ 10^5 J kg^{-1}
c_i	Specific heat capacity of ice	2.0 $\times$ 10^3 J kg^{-1} °C^{-1}
c_{oc}	Specific heat capacity of ocean	3974 J kg^{-1} °C^{-1}
λ_1	Liquidus slope	-5.75 $\times$ 10^{-2} °C PSU^{-1}
λ_2	Liquidus intercept	8.32 $\times$ 10^{-2} °C
λ_3	Liquidus pressure coefficient	7.59 $\times$ 10^{-4} °C m^{-1}
Box parameterisation		
$\beta_{S\star}$	Salt contraction coefficient	7.7 $\times$ 10^{-4} PSU^{-1}
$\beta_{T\star}$	Thermal expansion coefficient	7.5 $\times$ 10^{-5} °C^{-1}
ρ_*	EOS reference density	1033 kg m^{-3}
Plume parameterisation		
β_S	Salt contraction coefficient	7.86 $\times$ 10^{-4} PSU^{-1}
β_T	Thermal expansion coefficient	3.87 $\times$ 10^{-5} °C^{-1}
C_ϵ	Slope correction parameter	0.6
C_d	Drag coefficient	2.5 $\times$ 10^{-3}

We recognise the quadratic dependence of the melt rate to thermal forcing as used in previous formulations (Holland et al., 2008; DeConto and Pollard, 2016). We call this parameterisation the *quadratic-local* parameterisation in the following.

If we compare this new formulation with Eq. (7), this means that the turbulent exchange velocity now depends on the location
230 through the inclusion of the slope θ and on the far-field temperature T_{oc} and salinity S_{oc}:

$$\gamma_{TS,\text{loc},\theta} = C_d^{1/2} \Gamma_{TS} \frac{c_{oc}}{L_i} \beta_S S_{oc} \frac{g}{2 \, | \, f \, |} \sin\theta \epsilon (1 - \epsilon) \, | \, T_{oc} - T_{\text{f}} \, | \tag{15}$$

The remaining unknown parameter to tune is then:

$$K = C_d^{1/2} \Gamma_{TS} \epsilon (1 - \epsilon) \tag{16}$$

In formulations that do not explicitly include the slope, this means that a uniform slope $\sin\theta_{\text{Ant}}$ applicable to all Antarctica is
235 assumed. Otherwise, either the *local* slope θ_{loc}, for each point, or the *cavity* slope θ_{cav}, on the ice-shelf level, can be used. We estimate the local slope between the neighbouring grid cells in x- and y- directions at each ice-shelf point. The cavity slope is

estimated as the angle opened by the deepest grounding line point, the average ice draft depth at the ice shelf front, and the maximum distance between the grounding line and the ice shelf front.

Finally, in Eq. (11), the density deficit driving the buoyancy responsible for the vertical circulation depends on the local
240 thermal forcing. However, through the resulting circulation, the temperature at one point of the ice shelf cavity is not necessarily independent from the temperature at the other points of the ice shelf cavity. This is why Favier et al. (2019) proposed that the circulation should be driven by the averaged thermal forcing over the whole ice shelf instead. In our reformulation, this results in the following:

$$\gamma_{TS,\text{semiloc},\theta} = C_d^{1/2}\Gamma_{TS}\frac{c_{\text{oc}}}{L_i}\beta_S\langle S_{\text{oc}}\rangle\frac{g}{2\,|\,f\,|}\sin\theta\epsilon(1-\epsilon)\,|\,\langle T_{\text{oc}} - T_{\text{f}}\rangle\,| \tag{17}$$

245 and, when combined with Eq. (7) the following melt rate:

$$m = C_d^{1/2}\Gamma_{TS}\frac{\rho_{\text{oc}}}{\rho_{\text{i}}}\left(\frac{c_{\text{oc}}}{L_i}\right)^2\beta_S\langle S_{\text{oc}}\rangle\frac{g}{2\,|\,f\,|}\sin\theta\epsilon(1-\epsilon)\,|\,\langle T_{\text{oc}} - T_{\text{f}}\rangle\,|\,(T_{\text{oc}} - T_{\text{f}}) \tag{18}$$

We call this formulation the *quadratic-semilocal* parameterisation. If it is assumed that a constant θ_{Ant} can characterise all Antarctic ice shelves, this is analogous to the one proposed by Favier et al. (2019) and used as a standard parameterisation for ISMIP6 (Nowicki et al., 2020; Jourdain et al., 2020). If the local slope θ_{loc} is accounted for, this is analogous to the one used
250 in Lipscomb et al. (2021) and discussed by Little et al. (2009), Jenkins et al. (2018) and Jourdain et al. (2020).

Note that we made the choice here to parameterise U based on the assumption of a geostrophic circulation. We could also have parameterised it based on the assumption of a plume circulation (based on Sec. 2.2.2).

2.2.2 Plume parameterisation

More complex basal melting parameterisations aim to mimic the vertical overturning circulation in the cavity. The *plume pa-*
255 *rameterisation* describes the evolution of a 2-dimensional buoyant plume, originating at the grounding line with zero thickness and velocity. It evolves along the ice shelf base where it is affected by entrainment of ambient ocean water and melt at the ice-ocean interface. We implement it in two configurations. The first configuration of the plume parameterisation was initially proposed by Lazeroms et al. (2018). Here, we implement the revised, more physical, version described in Lazeroms et al. (2019). The second configuration of the plume parameterisation is a slightly modified version proposed for this particular
260 study, separating the effects of the temperature and velocity on the thermal forcing.

In both configurations, the melt rate m [in m ice per s] is computed as follows:

$$m = M_1 \cdot M_2 \cdot \frac{\rho_{\text{oc}}}{\rho_{\text{i}}} \tag{19}$$

using among others the parameters $c_{\rho 1}$ and c_τ, defined in Lazeroms et al. (2019):

$$c_{\rho 1} = \frac{L_i/c_{\text{oc}}}{C_d^{1/2}\Gamma_{TS}}\frac{\beta_T}{\beta_S S} \tag{20}$$

265

$$c_\tau = \frac{-\lambda_1 \beta_T/\beta_S}{c_{\rho 1}} \tag{21}$$

The two versions differ in the definition of the input temperature, salinity and slope used to compute M_1 and M_2. In the *Lazeroms* version, M_1 and M_2 are computed as follows:

$$M_1 = \left[\frac{\beta_S \mathbf{S_{cav}} g}{\lambda_3 (L_i/c_{\mathrm{oc}})^3}\right]^{1/2} \left[\frac{1 - \mathbf{c_{\rho 1,cav}} C_d^{1/2}\Gamma_{TS}}{C_d + E_0 \sin\theta_{\mathbf{loc}}}\right]^{1/2} \left[\frac{C_d^{1/2}\Gamma_{TS} E_0 \sin\theta_{\mathbf{loc}}}{C_d^{1/2}\Gamma_{TS} + \mathbf{c_{\tau,cav}} + E_0 \sin\theta_{\mathbf{loc}}}\right]^{3/2} \cdot (\mathbf{T_{cav}} - \mathbf{T_{f, gl}})^2 \tag{22}$$

270

$$M_2 = \frac{1}{2\sqrt{2}}[3(1-x)^{4/3} - 1]\sqrt{1 - (1-x)^{4/3}} \tag{23}$$

with the characteristic length scale:

$$x = \lambda_3 \frac{z_{\mathrm{draft}} - \mathbf{z_{gl}}}{\mathbf{T_{cav}} - \mathbf{T_{f,gl}}} \left[1 + C_\epsilon \left(\frac{E_0 \sin\theta_{\mathbf{loc}}}{C_d^{1/2}\Gamma_{TS} + \mathbf{c_{\tau,cav}} + E_0 \sin\theta_{\mathbf{loc}}}\right)^{3/4}\right]^{-1} \tag{24}$$

where E_0 is the entrainment coefficient, the subscript *cav* stands for the cavity mean, i.e. the far-field temperature and salinity
275 are extrapolated to the ice draft depth for each point and then averaged over the ice shelf area, θ_{loc} is the local slope, and the subscript *gl* stands for the effective grounding line depth. The local slope and effective grounding line depth are computed as described in Lazeroms et al. (2018), evaluating possible plume origins in 16 directions for each ice shelf point and averaging the local slope and grounding line depth, respectively, over the plausible plume origin directions. $c_{\rho 1,\mathrm{cav}}$ and $c_{\tau,\mathrm{cav}}$ are computed using S_{cav} as input for Eq. (20) and Eq. (21).

280   In the *modified* version, M_1 and M_2 are computed as follows:

$$M_1 = \left[\frac{\beta_S \mathbf{S_{loc}} g}{\lambda_3 (L_i/c_{\mathrm{oc}})^3}\right]^{1/2} \left[\frac{1 - \mathbf{c_{\rho 1,loc}} C_d^{1/2}\Gamma_{TS}}{C_d + E_0 \sin\theta_{\mathbf{loc}}}\right]^{1/2} \left[\frac{C_d^{1/2}\Gamma_{TS} E_0 \sin\theta_{\mathbf{loc}}}{C_d^{1/2}\Gamma_{TS} + \mathbf{c_{\tau,loc}} + E_0 \sin\theta_{\mathbf{loc}}}\right]^{1/2} \cdot (\mathbf{T_{loc}} - \mathbf{T_{f, loc}})$$
$$\cdot \left[\frac{C_d^{1/2}\Gamma_{TS} E_0 \sin\theta_{\mathbf{loc}}}{C_d^{1/2}\Gamma_{TS} + \mathbf{c_{\tau,ups}} + E_0 \sin\theta_{\mathbf{loc}}}\right] \cdot (\mathbf{T_{ups}} - \mathbf{T_{f,ups,gl}})$$

285 $$M_2 = \frac{1}{2\sqrt{2}}[3(1-x)^{4/3} - 1]\sqrt{1 - (1-x)^{4/3}} \tag{25}$$

with the characteristic length scale:

$$x = \lambda_3 \frac{z_{\mathrm{draft}} - \mathbf{z_{deepest\ gl}}}{\mathbf{T_{cav}} - \mathbf{T_{f, deepest\ gl}}} \left[1 + C_\epsilon \left(\frac{E_0 \sin\theta_{\mathbf{cav}}}{C_d^{1/2}\Gamma_{TS} + \mathbf{c_{\tau,cav}} + E_0 \sin\theta_{\mathbf{cav}}}\right)^{3/4}\right]^{-1} \tag{26}$$

where the subscript *loc* stands for the far-field properties extrapolated to the local ice draft depth, and the subscript *ups* stands for the upstream mean of the properties, i.e. the mean, for each point of the ice shelf, of the properties between local ice draft

290   depth and local effective grounding line depth in the input profiles, the subscript *deepest gl* stands for the deepest grounding line point, and θ_{cav} stands for the cavity slope (estimated as described in Sec. 2.2.1). $c_{\rho1,\mathrm{loc}}$ and $c_{\tau,\mathrm{loc}}$ are computed using S_{loc}, as input for Eq. (20) and Eq. (21), and $c_{\rho1,\mathrm{ups}}$ and $c_{\tau,\mathrm{ups}}$ using S_{ups}. In this version, the last factor of M_1 is divided into the part driven by the velocity scale (on the local scale, *loc*) and the temperature scale (upstream mean, *ups*)

In the plume parameterisation, two parameters can be tuned: the effective thermal Stanton number $C_d^{1/2}\Gamma_{TS}$ and the entrain-
295   ment coefficient E_0.

2.2.3   Box parameterisation

The *box parameterisation* was originally proposed by Olbers and Hellmer (2010) and further developed as *PICO* by Reese et al. (2018). It simulates the overturning transport of heat and salt from the far field to the grounding line, and then along the ice-ocean interface up to the front. We divide each ice-shelf domain into several boxes, which are defined based on the relative
300   distance between the closest ice-shelf front and the closest grounding line point. The division into boxes for each ice shelf is done following the criteria given in Reese et al. (2018), depending on r, the non-dimensional relative distance to the grounding line at each point:

$$r = d_{\mathrm{GL}}/(d_{\mathrm{GL}} + d_{\mathrm{IF}}) \tag{27}$$

and a grid point belongs to box k if:

305    $$1 - \sqrt{(n_D - k + 1)/n_D} \leq r \leq 1 - \sqrt{(n_D - k)/n_D} \tag{28}$$

where d_{GL} and d_{IF} are the distance between the ice shelf point and the nearest grounding line point on the one hand and between the ice shelf point and the nearest ice shelf front point on the other hand, n_D is the total number of boxes, and $k \in [1, n_D]$.

We use the criterion given by Reese et al. (2018) to define the amount of boxes for each ice shelf, resulting in an amount of boxes between 2 and 5 (see Table C1, last column), similar to the configuration used in PICO, and called *PICO boxes* in
310   the following. Favier et al. (2019) showed that melt rates do not necessarily converge above 5 boxes. Therefore, we investigate three additional box setups: one with two boxes, one with five boxes, and one with ten boxes. If one of the boxes has an area of zero or if the slope between two boxes is negative in the direction from the grounding line to the ice shelf front, we apply a smaller number of boxes in the given setup until all boxes are non-zero and the slope between all boxes is positive. When such correction is needed, we enforce that $n_{\mathrm{D,\,10\,boxes}} > n_{\mathrm{D,\,5\,boxes}} > n_{\mathrm{D,\,2\,boxes}}$, with 1 box being the lowest amount possible. The
315   resulting amount of boxes in each setup is shown in Table C1.

The far-field properties at the average entrance depth of each ice-shelf cavity are advected to the grounding line. This is slightly different from Reese et al. (2018) who consider the sea-floor temperature on the scale of larger basins. Then, the far-field water mixes with meltwater and rises up along the ice-shelf base due to buoyancy. In contrast to plume models (e.g. Jenkins, 1991), entrainment of deeper water is neglected. Assuming steady state, the temperature T_k and salinity S_k for the

box k (k increasing from the grounding line to the ice shelf front) depend on the temperature T_{k-1} and the salinity S_{k-1} in the previous box, the area A_k of the current box, the melt m_k in the current box and the overturning flux q :

$$
\begin{aligned}
0 &= q(T_{k-1} - T_k) - A_k m_k \left(\frac{\rho_{\mathrm{oc}} c_{\mathrm{oc}}}{\rho_{\mathrm{i}} L_{\mathrm{i}}} \right) \\
0 &= q(S_{k-1} - S_k) - A_k m_k S_k
\end{aligned}
\tag{29}
$$

with the overturning flux calculated as:

$$
q = C \rho_\star [\beta_{S\star}(S_0 - S_1) - \beta_{T\star}(T_0 - T_1)]
\tag{30}
$$

where C is the overturning strength, $\rho_\star$ is the reference density for the haline contraction coefficient $\beta_{S\star}$ and the thermal expansion coefficient $\beta_{T\star}$ (see Table 2).

Finally, the melt [in m ice per s] is computed similarly to Eq. (7) for each box:

$$
m_k = \gamma_T^\star \left(\frac{\rho_{\mathrm{oc}} c_{\mathrm{oc}}}{\rho_{\mathrm{i}} L_{\mathrm{i}}} \right) (T_k - T_{f,k})
\tag{31}
$$

where $\gamma_T^\star$ is the effective turbulent temperature exchange velocity, assumed to be constant and uniform, like in the *linear-local* parameterisation, which also contrasts with most plume models (e.g. Jenkins, 1991). $T_{f,k}$ is the freezing point in box k. $T_{f,k}$ can either be assumed as constant, computed based on the mean depth of the box (homogeneous boxes in the following), or can be assumed as depth-dependent at each ice-draft point, computed based on the local ice-draft depth (heterogeneous boxes in the following). A more detailed description of the equations underlying the box parameterisation can be found in Reese et al. (2018). In the box parameterisation, there are two parameters to be tuned: the overturning coefficient C and the effective turbulent temperature exchange velocity $\gamma_T^\star$.

2.2.4 PICOP parameterisation

The *PICOP parameterisation* is a combination of the box and plume parameterisation (Pelle et al., 2019). The temperature and salinity in the ice shelf cavity are computed using PICO (Reese et al., 2018). This temperature and salinity are then used as input for the plume parameterisation as described in Lazeroms et al. (2018). In that plume formulation, M_2 is not described by an analytical function like in Eq. (23) but by a polynomial (see Eq. (A13), Eq. (A10), and Eq. (A11) in Lazeroms et al. (2018)). We use all parameters as defined in Lazeroms et al. (2018) and Pelle et al. (2019), except $C_d^{1/2}\Gamma_T$ which we change to 7×10^{-5} following personal communication with T. Pelle. Unlike in Pelle et al. (2019), we use the effective grounding line depth as in Lazeroms et al. (2018), while Pelle et al. (2019) computed it through a pathway following the ice advection.

In Lazeroms et al. (2018), $C_d^{1/2}\Gamma_{TS}$ was computed based on other fixed parameters. For our re-tuning, we therefore use the plume implementation from Lazeroms et al. (2019). This way, all four parameters $\gamma_{T}\star$, C, $C_d^{1/2}\Gamma_{TS}$, and E_0 can in principle be tuned here. To reduce complexity, we choose to use the tuned $\gamma_{T}\star$ and C, and only re-tune $C_d^{1/2}\Gamma_{TS}$, and E_0.

2.3 Input profiles to the parameterisations

We compute a mean potential temperature and a mean practical salinity profile in front of each ice shelf to be used as "far-field" input to the different parameterisations. We use yearly mean profiles as the residence time of water in ice shelf cavities might be longer than a month for some cavities. For each ice shelf, we sample all grid points within a given distance of the ice shelf front and compute the mean over all such grid points. To study the sensitivity of the tuning to the size of the chosen domain, we define four different domain sizes encompassing all grid points on the continental shelf, defined as points where the depth of the bathymetry is shallower than 1500 m, within 10, 25, 50 and 100 km of the ice shelf front respectively. Additionally, to mimic the coarse resolution of some global climate models, e.g. some of the CMIP or PMIP models (Paleoclimate Modelling Intercomparison Project, Kageyama et al., 2018), that do not properly resolve the continental shelf or associated processes, we define an additional domain, which we call "offshore" domain. This domain is defined as all ocean points within $10°$ of longitude and $3.5°$ of latitude from the ice shelf front and with a bathymetry deeper than 1500m, i.e. we exclude the points on the continental shelf. The offshore domain size is two times the effective resolution of a typical climate model, which we assume to be $5.0° \times 1.75°$ at $70°$S, i.e. $\sim 5\Delta x$ for a model of $1°$ resolution in longitude.

In most cases, there is no clear visible difference between the profiles averaged over 10, 25, 50 and 100 km (REALISTIC simulation shown as example in Fig. 2) but there is a clear difference between these domains and the offshore domains. As a consequence, for the further analysis, we will keep the diversity introduced by the four simulations of the ensemble (Fig. 1) to introduce variability in our forcing but we will only focus on one domain over the continental shelf and one over the offshore domain. We choose the 50 km domain as most CMIP-type global ocean models have resolutions around $1°$ (Heuzé, 2021) and this corresponds to a distance of between 38 km ($70°$S) and 56 km ($60°$S) in longitude.

2.4 Tuning approach

To re-tune the parameterisations presented in Sec. 2.2, we minimise the root-mean-squared error (RMSE) between the simulated and parameterised yearly integrated melt (M) of the individual ice shelves (in Gt/yr) and simulated years (Fig. 3) as follows:

$$RMSE_{\text{int}} = \sqrt{\frac{\sum_i^{N_{\text{isf}}} \sum_t^{N_{\text{years}}} (M_{\text{param}}[i,t] - M_{\text{ref}}[i,t])^2}{N_{\text{isf}} N_{\text{years}}}} \tag{32}$$

where N_{isf}=36 is the number of ice shelves and N_{years}=127 the number of simulated years. We do so for each input domain (i.e. the 50 km and the offshore domain) separately.

The simple parameterisations are based on a linear relationship between the far-field properties and the basal melt. Therefore, for each of them, we compute a thermal forcing factor containing all information that is multiplied with the tuneable parameter, and fit it to the simulated melt via a least-squares regression. The resulting slope is the tuned parameter $\gamma_{TS,\text{loc, Ant}}$ for the *linear-local* parameterisations and K for the other simple parameterisations (see Eq. (16)).

The plume and the box parameterisation are more complex and each have two parameters to be tuned: $(\Gamma_{T,S}, E_0)$ and $(\gamma_T^\star, C)$ respectively. The PICOP has all these four parameters to be tuned. For simplification, we take the newly tuned box parameters

Figure 2. Comparison of mean input temperature profiles between the five different domains which were averaged (10, 25, 50, 100 km and offshore) in one given simulation (REALISTIC). The shading represents the interannual variability (one standard deviation over time). The horizontal dotted lines show the average depth of the bed at the ice front (light brown), the largest depth of the bed at the ice front (dark brown) and the largest depth of the grounding line (grey).

$(\gamma_T^\star, C)$ and only tune the plume parameters $(\Gamma_{T,S}, E_0)$. For the plume and PICOP parameterisation, we use a Trust Region

380 Reflective algorithm (Branch et al., 1999), which loops over different parameter choices within given bounds (here we aim for positive parameters) and minimises the RMSE step by step. For the parameters of the box parameterisation, two constraints
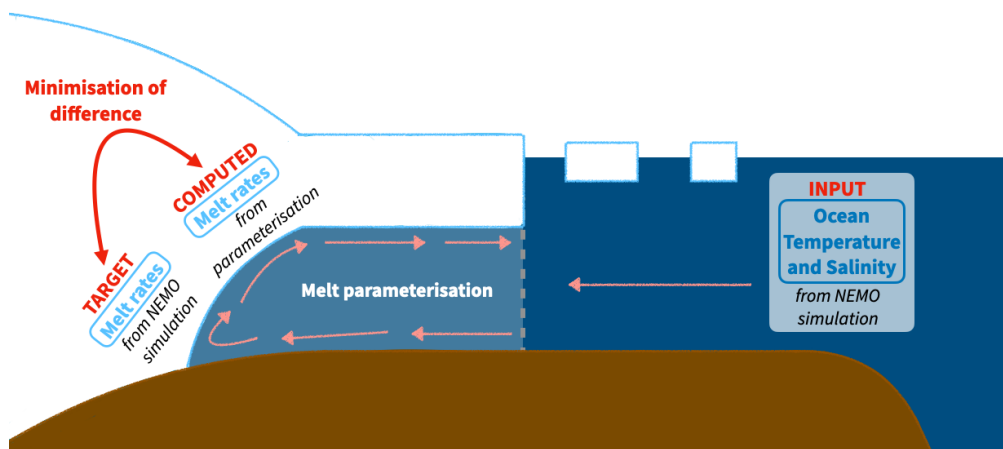
Figure 3. Schematic of the perfect model approach to assess the different parameterisations.

are additionally needed, namely that the melt in first box should always be positive and that the melt in box 1 should always be more than the melt in box 2 (Reese et al., 2018). This is why we apply a Sequential Least Squares Programming algorithm (Kraft, 1988), which allows the definition of such constraints. Both algorithms are implemented in the python scipy package

385 (Virtanen et al., 2020). To ensure that the algorithms search for physically sensible parameters, we provide physically-informed bounds and use the parameters given by the previous literature as initial guesses.

3 Results

We assess the re-tuned parameterisations in two steps. First, we evaluate the performance of the parameterisations in representing the integrated ice-shelf melt, using the parameters suggested in previous work and the newly tuned parameters. Second,

390 we examine the performance of the tuned parameterisations in regard to the spatial distribution of the melt. Note that we only discuss circum-Antarctic results. For the metrics on the level of the individual ice shelves, refer to Appendix D.

3.1 Evaluation of the parameterised integrated ice-shelf melt

3.1.1 Simple parameterisations

The tuning of the simple parameterisations results in the parameters shown in Table 3, for the 50 km and the offshore domain

395 respectively. The root-mean-squared error (RMSE) between the parameterised and reference integrated melt for the simple parameterisations is shown in Table 4.

   Using the newly tuned parameters with hydrographic input from the 50 km domain clearly improves the representation of the sub-shelf integrated melt compared to the use of parameters suggested by Favier et al. (2019) and the "PIGL" recommendation for ISMIP6 by Jourdain et al. (2020)(Table 4, 1st and 3rd column). While the original parameters result in an RMSE between

Table 3. Summary of the tuned parameters ($\gamma_{TS,\text{loc, Ant}}$ and K) for the simple parameterisations, see Eq. (9) and Eq. (16). For the Antarctic slope parameterisations, K is inferred by assuming that $\sin\theta_{\text{Ant}} = 2.9\times10^{-3}$, which is the average over all local slopes in our virtual reality.

Parameterisation	$\gamma_{TS,\text{loc, Ant}}$ or K	$\gamma_{TS,\text{loc, Ant}}$ or K
	Tuned (50 km)	Tuned (offshore)
Linear-local	2.5×10^{-6}	0.29×10^{-6}
Quadratic-local Ant slope	11.8×10^{-5}	0.24×10^{-5}
Quadratic-local cavity slope	6.6×10^{-5}	0.72×10^{-5}
Quadratic-local local slope	9.0×10^{-5}	0.37×10^{-5}
Quadratic-semilocal Ant slope	13.0×10^{-5}	0.25×10^{-5}
Quadratic-semilocal cavity slope	6.3×10^{-5}	0.71×10^{-5}
Quadratic-semilocal local slope	9.3×10^{-5}	0.38×10^{-5}

400 177 and 992 Gt/yr, the tuned parameters lead to an RMSE between 29.7 and 54.9 Gt/yr. Note that the "PIGL" recommendation goes hand-in-hand with local temperature corrections, which are negative for the majority of basins (Jourdain et al., 2020), so the high RMSE here is not necessarily surprising in the absence of temperature corrections. In contrast, the parameters proposed by Jourdain et al. (2020) for the "MeanAnt" case in ISMIP6 considerably reduce the difference between the parameterised and the reference melt (Table 4, 2nd column), especially for the quadratic-semilocal formulation including the local slope. The new
405 tuning only slightly achieves to reduce the RMSE further.

The comparison between the parameterised and reference melt for the tuned simple parameterisations shows that comparably low RMSE, on the order of 30 Gt/yr, are obtained for the quadratic versions of the parameterisation when using a constant Antarctic slope or including the local slope (Table 4, 4th column). Using the cavity slope as slope information or the linear-local parameterisation leads to comparably higher RMSE, on the order of 50 Gt/yr.
410 Even with parameters tuned specifically with offshore properties, the RMSE between the melt parameterised using offshore properties and the reference melt is 6 to 35 Gt/yr higher than when using input from the 50 km domain (Table 4, last column). In this case, the RMSE is lowest when applying quadratic formulations using the cavity slope.

Table 4. Root-mean squared error between the reference (NEMO) and parameterised (simple parameterisations) yearly integrated ice-shelf melt [Gt/yr] over the 36 individual ice shelves and 127 simulation years using the parameters from Favier (Favier et al., 2019) (1st column), ISMIP6 (Jourdain et al., 2020) (2nd and 3rd column) and tuned (4th column), with input properties from the 50 km domain. The 5th column uses the tuned parameters and the input from the offshore domain. The RMSE combining offshore properties and parameters from previous studies are not shown because they are one to three orders of magnitude higher.

Parameterisation	Favier 2019 (50 km)	ISMIP6 MeanAnt (50 km)	ISMIP6 PIGL (50 km)	tuned (50 km)	tuned (offshore)
Linear-local	350.9			54.9	64.5
Quadratic-local Ant slope	176.7	35.0	315.4	30.2	64.9
Quadratic-local cavity slope				50.1	56.1
Quadratic-local local slope				32.8	61.5
Quadratic-semilocal Ant slope	213.8	41.0	991.7	29.7	65.0
Quadratic-semilocal cavity slope				47.9	56.1
Quadratic-semilocal local slope		32.8	84.6	31.0	61.5

Table 5. Comparison between original (from Lazeroms et al., 2019) and tuned parameters for the plume parameterisation. "Lazeroms" refers to the version from Lazeroms et al. (2019) and "modified" to the modified version, both presented in Sec. 2.2.2. The values in italic are subject to caution (see text).

Parameterisation	$C_d^{1/2}\Gamma_{TS}$	E_0	$C_d^{1/2}\Gamma_{TS}$	E_0	$C_d^{1/2}\Gamma_{TS}$	E_0
	Lazeroms	Lazeroms	tuned (50 km)	tuned (50 km)	tuned (offshore)	tuned (offshore)
Lazeroms formulation	5.9×10^{-4}	3.6×10^{-2}	2.1×10^{-4}	5.4×10^{-2}	10.4×10^{-4}	0.39×10^{-2}
Modified version	5.9×10^{-4}	3.6×10^{-2}	1.3×10^{-4}	7.2×10^{-2}	9.3×10^2	0.16×10^{-2}

Table 6. Root-mean squared error between the reference (NEMO) and parameterised (plume parameterisation) yearly integrated ice-shelf melt [Gt/yr] for the 36 individual ice shelves and 127 simulation years using the original parameters (Lazeroms et al., 2019) and the tuned parameters. RMSE is given for the Lazeroms formulation (Lazeroms et al., 2019) and the modified version.

Version	original (50 km)	tuned (50 km)	tuned (offshore)
Lazeroms version	43.6	35.2	59.8
Modified version	102.5	35.0	62.5

3.1.2 Plume parameterisation

The newly tuned parameters for the plume parameterisation (shown in Table 5) using 50 km domain input properties are on
a similar order of magnitude as the previously suggested parameters. Using the original parameters for the modified version
leads to a more than doubled RMSE compared to the Lazeroms version (Table 6, 1st column). After tuning, the RMSE is
comparable between the two versions, around 35 Gt/yr for the 50 km domain (Table 6, 2nd column).

Using the offshore input properties in combination with the tuned parameters for offshore results in a RMSE around 60 Gt/yr.
For the Lazeroms version, the Stanton Number is one order of magnitude higher than for the 50 km domain, while the entrain-
ment coefficient is one order of magnitude lower. For the modified version, however, the Stanton number is on the order of
10^2 instead of 10^{-4}. We cannot pinpoint to the exact reason for this large difference in order of magnitude but conjecture that
it is related to the behaviour of the modified version on large ice shelves in conjunction with larger thermal forcing from the
offshore domain compared to the 50 km domain.

Table 7. Comparison between original (from Reese et al., 2018) and tuned parameters for the box parameterisation for the different setups, using heterogeneous boxes.

Maximum number of boxes	$\gamma_T^\star$ original	C original	$\gamma_T^\star$ tuned (50 km)	C tuned (50 km)	$\gamma_T^\star$ tuned (offshore)	C tuned (offshore)
2 boxes	2×10^{-5}	1×10^6	0.40×10^{-5}	12.1×10^6	0.56×10^{-5}	0.13×10^6
5 boxes	2×10^{-5}	1×10^6	0.43×10^{-5}	12.9×10^6	0.82×10^{-5}	0.12×10^6
10 boxes	2×10^{-5}	1×10^6	0.47×10^{-5}	14.4×10^6	1.02×10^{-5}	0.13×10^6
PICO boxes	2×10^{-5}	1×10^6	0.41×10^{-5}	15.1×10^6	0.70×10^{-5}	0.12×10^6

3.1.3 Box parameterisation

425 For the 50 km domain, the newly tuned $\gamma_T^\star$ is an order of magnitude lower than in Reese et al. (2018) (Table 7, 3rd and 4th column), but on a similar order of magnitude as our tuned $\gamma_{TS,\mathrm{loc},Ant}$ for the linear-local parameterisation (see Table 3). The newly tuned overturning coefficient C is ten times higher than the original value. In Reese et al. (2018), C was bound at the higher end through the constraint that the mean melt in box 2 has to be lower than the mean melt in box 1. In our case, this constraint did not lead to an upper bound for C, which might be a consequence of different input temperatures compared to Reese et al. (2018). The tuned $\gamma_T^\star$ and C do not differ significantly between the homogeneous and heterogeneous boxes

430 approach. We therefore only show results for heterogeneous boxes hereafter.

With values varying only slightly between 43.7 and 45.1 Gt/yr, the RMSE between the parameterised and reference integrated melt using the tuned parameters for the 50 km domain is considerably reduced compared to the RMSE using the original parameters from Reese et al. (2018) (Table 8, 3rd column). Increasing the number of boxes slightly improves the parameterised

435 melt but the difference between the different setups remains small. This might be explained by the fact that we tune the parameters for each setup separately, resulting in the optimal parameters for each setup (Table 7), adapting to the difference in the amount of boxes.

The tuned parameters using the input from the offshore domain are distributed differently. $\gamma_T^\star$ is about twice as high than the tuned $\gamma_T^\star$ for the 50 km domain, while C is now one order of magnitude lower than the original C, i.e. two orders of magnitude

440 lower than the C tuned for the 50 km domain (Table 7, 5th and 6th column). The resulting RMSE between parameterised and reference melt is around 10 Gt/yr higher than for the 50 km domain (Table 8, 4th column).

Table 8. Root-mean squared error between the reference (NEMO) and parameterised (box parameterisation) yearly integrated ice-shelf melt [Gt/yr] over the 36 individual ice shelves and 127 simulation years using the original parameters (Reese et al., 2018) and the tuned parameters (tuned separately for each configuration). RMSE is given for the version with heterogeneous boxes, and for the use of input from the 50 km and the offshore domains.

Maximum number of boxes	original (50 km)	tuned (50 km)	tuned (offshore)
2 boxes	81.8	45.1	54.5
5 boxes	68.0	44.5	53.5
10 boxes	58.9	43.7	52.5
PICO boxes	72.7	45.0	54.2

Table 9. Comparison between original and tuned parameters for the PICOP parameterisation. These are the plume parameters, the box parameters are the tuned parameters shown in Table 7.

PICOP setup	$C_d^{1/2}\Gamma_{TS}$	E_0	$C_d^{1/2}\Gamma_{TS}$	E_0	$C_d^{1/2}\Gamma_{TS}$	E_0
	Lazeroms	Lazeroms	tuned (50 km)	tuned (50 km)	tuned (offshore)	tuned (offshore)
10 boxes, heterogeneous	5.9×10^{-4}	3.6×10^{-2}	1.3×10^{-4}	3.6×10^{-2}	2.3×10^{-4}	5.6×10^{-2}
PICO boxes, homogeneous	5.9×10^{-4}	3.6×10^{-2}	1.8×10^{-4}	2.2×10^{-2}	1.4×10^{-4}	8.9×10^{-2}

Table 10. Root-mean squared error between the reference (NEMO) and parameterised (PICOP parameterisation) yearly integrated ice-shelf melt [Gt/yr] over the 36 individual ice shelves and 127 simulation years using the original parameters (Reese et al., 2018; Lazeroms et al., 2019) and the tuned parameters (tuned separately for each configuration).

PICOP setup	original (50 km)	tuned (50 km)	tuned (offshore)
10 boxes, heterogeneous	138.8	48.3	62.6
PICO boxes, homogeneous	176.9	49.5	63.9

3.1.4 PICOP parameterisation

For the PICOP parameterisation, we use the tuned box parameters (see Table 7) and re-tune the plume parameters only (see Table 9). We showed in Sec. 3.1.3 that the RMSE remains similar between the different amount of boxes and when using the homogeneous and heterogeneous boxes. Therefore, we reduce the diversity of setups for the PICOP tuning. We keep the version using the PICO amount of boxes and the homogeneous boxes, as this is the original implementation in Pelle et al. (2019), and we keep a version using the 10-box setup and heterogeneous boxes, as this setup results in the lowest RMSE for the box parameterisation (see Table 8).

The resulting parameters are all on a similar order of magnitude as the original ones (Table 9). In the PICO, homogeneous version, the entrainment coefficient is about three times as high in the offshore tuning compared to the 50 km tuning, while the Stanton number is comparable in both cases. In the 10-box, heterogeneous version, the entrainment coefficient is about twice as high in the offshore case as in the 50 km case and the Stanton number slightly increases between the two. In both cases, the use of the tuned parameters considerably reduces the RMSE between parameterised and reference melt (Table 10). Slightly above 60 Gt/yr, the RMSE for the offshore input is about 10 Gt/yr higher than for the 50 km domain (between 48.3 and 49.5 Gt/yr).

3.1.5 Summary

The RMSE of the integrated melt over the 36 individual ice shelves and 127 simulation years is summarised for all tuned parameterisations in Fig. 4. To put these RMSE in context, the integrated ice-shelf melt averaged over all ice shelves and simulation years in the reference is 38 Gt/yr, which means that even for the better-performing parameterisations, the RMSE remains very high compared to the reference melt as such. For the 50 km domain, the lowest RMSE in the integrated ice-shelf

melt, on the order of 30 to 35 Gt/yr) is found for the simple quadratic parameterisations using a constant Antarctic slope or the local slope, and for the plume parameterisation.

Using offshore properties, even with specifically tuned parameters, substantially increases the RMSE, now reaching 52.5 to 65.0 Gt/yr. In this combination, the lowest RMSE is found for the parameterisations performing less well in the 50 km domain,

465   such as the simple quadratic formulation using the cavity slope and the box parameterisation. The increase in RMSE for the offshore domain confirms the importance of using hydrographic properties from the continental shelf to reduce uncertainties, as recommended by Dinniman et al. (2016) and Asay-Davis et al. (2017). As a consequence, in the following, for the evaluation of spatial patterns, we only concentrate further on the 50 km domain.
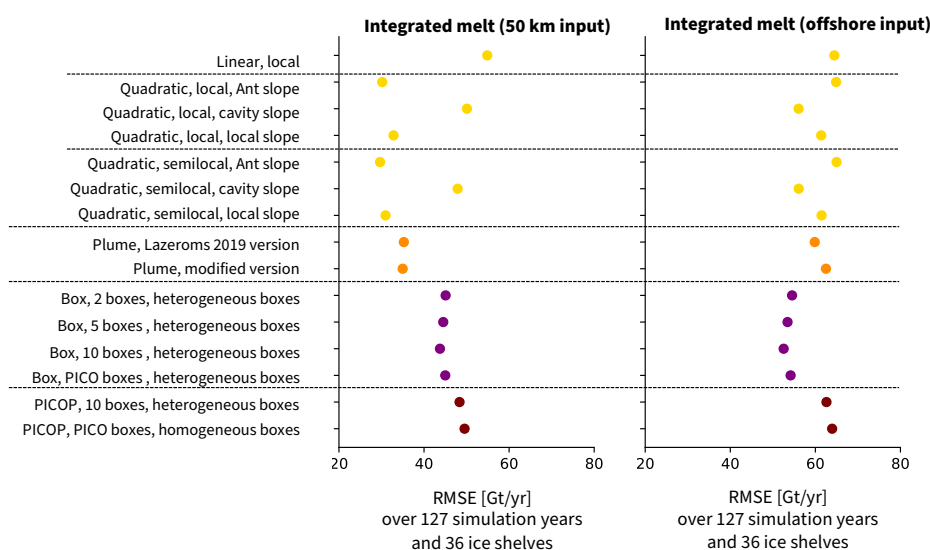
Figure 4. Summary of the RMSE of the integrated melt [in Gt/yr] over the 36 individual ice shelves and the 127 simulation years for a selection of parameterisations, using the 50 km domain (left) and the offshore domain (right). The colors represent the different parameterisation approaches: simple (yellow), plume (orange), box (purple), PICOP (brown). The RMSE is computed following Eq.(32) in both panels.

3.2 Evaluation of the spatial melt patterns

470 While Joughin et al. (2021) suggest that the integrated melt is the main driver for grounding line retreat, other studies suggest that ice-sheet models are more sensitive to melt rates near the grounding line than to cavity-integrated melt rates (e.g. Gagliardini et al., 2010; Morlighem et al., 2021). Therefore simulating realistic melt patterns, especially near the grounding line, might be at least as important as simulating a realistic integrated melt. To assess the parameterisations from another perspective, we investigate their ability to represent time-averaged melt patterns. First, we visually assess the difference between the parame-
475 terised and the reference melt pattern. Then, we quantify differences in these time-averaged melt rates near the grounding line between parameterisations and reference through the RMSE.

3.2.1 Visual evaluations

The circum-Antarctic time-averaged pattern for a subset of parameterisations applied to the REALISTIC simulation is shown in Fig. 5. The subset represents the respective configurations of the parameterisations that yield a comparatively lower RMSE
480 in the integrated melt (see Sec. 3.1).

   At first sight, all parameterisations lead to reasonable results compared to the reference. Differences can mainly be seen in terms of refreezing. While the simple parameterisations do not exhibit any refreezing, the plume parameterisation leads to some refreezing under the Filchner-Ronne ice shelf, and the boxes and PICOP lead to large refreezing areas under both the Filchner-Ronne and Ross ice shelves. Also, in the box parameterisation, the melt in the Amundsen Sea is homogeneous for the
485 different ice shelves, while the other parameterisations better represent strong melting for the Pine Island, Thwaites, and Getz ice shelves, and lower melting for the others.

   For a more detailed overview on the ice-shelf level, the time-averaged patterns of a subset of ice shelves, representative for different regions, are shown in Fig. 6. These include the three largest ice shelves Filchner-Ronne, Ross, and Amery; the ice shelf in front of Pine Island Glacier in the Amundsen Sea; the Fimbul ice shelf located at the outskirts of Dronning Maud
490 Land; and Totten ice shelf, located in the East. It becomes clear that the melt patterns are very different on the ice-shelf level depending on the parameterisation. For example, the quadratic local parameterisation using a constant Antarctic slope tends to have a smoother pattern than the quadratic semilocal parameterisation using a local slope. The latter leads to locally very high melt rates, substantially higher than the reference (e.g. for Pine Island or Totten), which could explain the high RMSE for the melt near the grounding line (see Fig. 7). For this given subset of ice shelves, the Lazeroms verison of the plume
495 parameterisation captures some patterns better than the modified version (e.g. Filchner-Ronne, Pine Island, Amery). Both plume parameterisations overestimate the melt for Totten Ice Shelf. The box parameterisation exhibits its signature pattern, i.e. decreasing melt from the grounding line to the ice front for all ice shelves, however the melt remains generally lower than the reference, except for the Fimbul Ice Shelf. Finally, PICOP combines the advantages and disadvantages of the box and plume parameterisations, for example with large areas of refreezing under the Filchner-Ronne ice shelf, but patterns comparable to
500 the reference for Pine Island, Amery and Totten.

For the Ross ice shelf, the simple and plume parameterisations exhibit melting over too large areas compared to the reference, while the box and PICOP parameterisation exhibit freezing over too large areas. Finally, for the Fimbul Ice Shelf, the reference shows strong melting near the ice front. This is a result of a seasonal melt cycle, with melt near the front during summer (Jacobs et al., 1992, third mode of melting described by). None of the parameterisations matches the reference pattern, likely because they are all forced by yearly ocean temperatures.

3.2.2 Statistical evaluation

To quantify the performance of the different parameterisations, additionally to the visual evaluation, we compute the RMSE between reference and parameterised melt near the grounding line (m_{GL}). To do so, we define the melt near the grounding line as the melt in the region defined through the first box of the box parameterisation in the 5-box setup, which represents ≈10% of the ice shelf area. Here we use average melt rates m (in m ice/yr) rather than integrated melt M (in Gt/yr) used in the previous section to have a complementary metric and to evaluate more the skills to represent regional contrasts in local melt intensity near grounding lines:

$$RMSE_{\mathrm{GL}} = \sqrt{\frac{\sum\limits_{i}^{N_{\mathrm{isf}}} \sum\limits_{n}^{N_{\mathrm{simu}}} (m_{\mathrm{GL,param}}[i,n] - m_{\mathrm{GL, ref}}[i,n])^2}{N_{\mathrm{isf}} N_{\mathrm{simu}}}} \tag{33}$$

where N_{simu}=4 is the number of simulations in the ensemble.

The results are shown, alongside the previously presented RMSE for the integrated melt, in Fig. 7. Here again, for some context, we compute the average melt near the grounding line over all ice shelves and simulations, resulting in 0.44 m ice/yr. This means that, in this case too, the RMSE is high compared to the reference melt as such. Like for the integrated melt, the simple quadratic parameterisations using a constant Antarctic slope and the plume parameterisation lead to the lowest RMSE. However, using a local slope leads to a strong increase in the RMSE. This can be explained by punctual very strong melt, as seen in Fig. 6 for Ross, Pine Island, and Totten for example. While the local slope leads to reasonable results in the integrated melt, it should therefore be kept in mind that it can induce an overestimation of the melt on a local scale. On the opposite, PICOP does not perform well on the integrated melt scale but very well for the melt rate near the grounding line, even better than the simple quadratic and plume parameterisations. This suggests that the combination of box and plume parameterisation is useful for parameterising the melt near the grounding line.
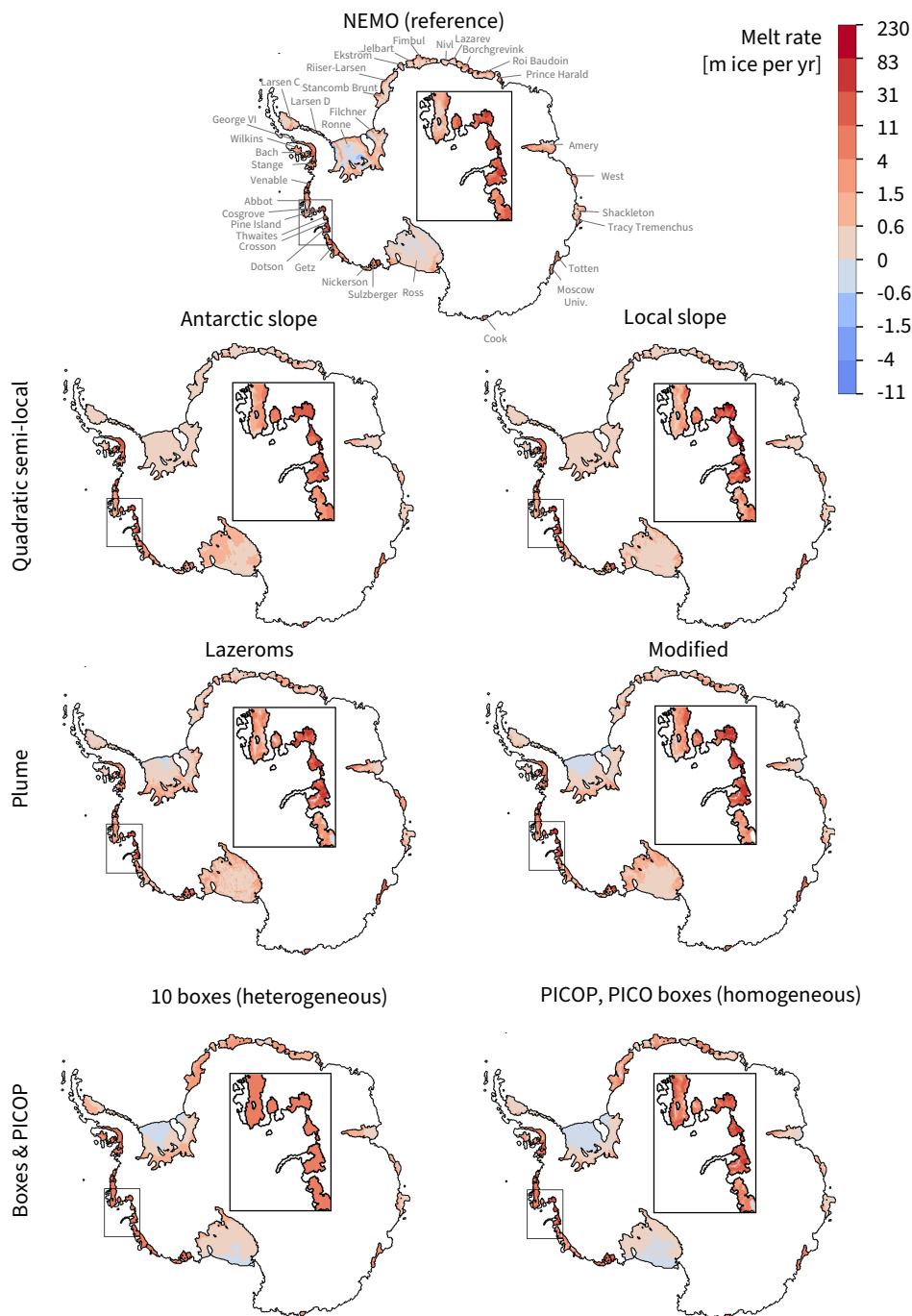
Figure 5. Spatial distribution of the yearly melt for a subset of the tuned parameterisations and for the reference for comparison. This is the time average for the REALISTIC run (39 years). Note that the land tongue in the Amundsen Sea was introduced to mimic the effect of grounded icebergs present in that region on the sea-ice circulation (see Sec. 2.1.2).
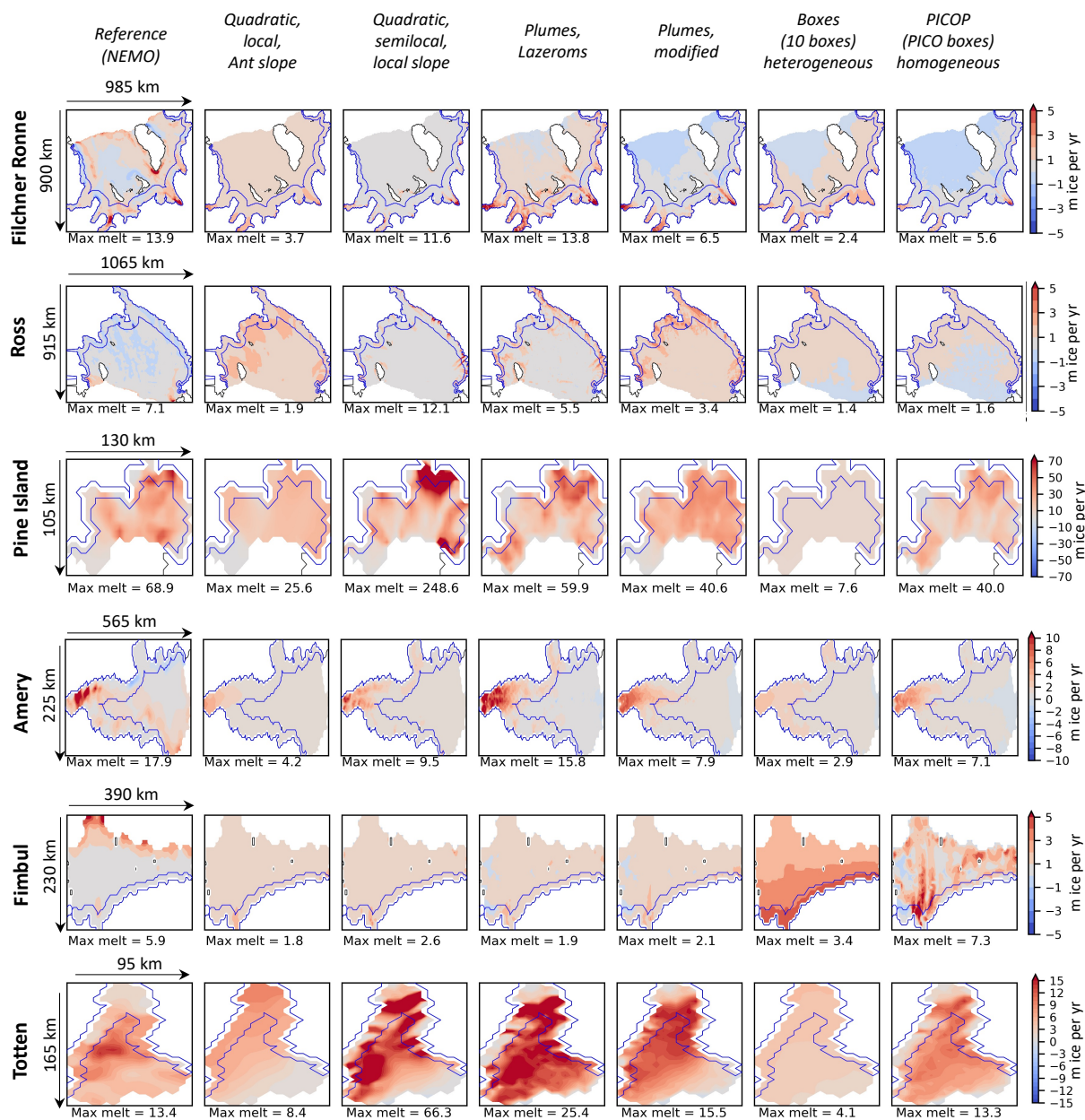
Figure 6. Subset of ice shelves for a visual evaluation of the melt patterns. This is the time average for the REALISTIC run (39 years). The blue line indicates the region used to evaluate the melt rate near the grounding line (which is defined as the first box in the 5-box setup of the box parameterisation).
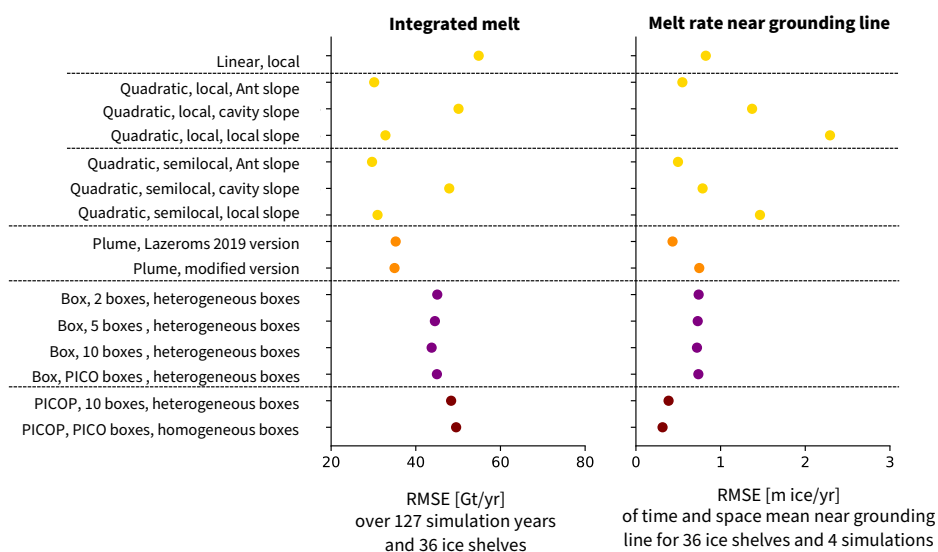
Figure 7. Summary of the RMSE of the integrated melt over the 36 individual ice shelves and the 127 simulation years for a selection of parameterisations, using the 50 km domain, [in Gt/yr] (left, same as Fig. 4 left) and summary of the RMSE of the melt averaged over time and space near the grounding line (average in the first box of the 5-box setup) over the 36 individual ice shelves and four simulations [in m ice/yr] (right). The colors represent the different parameterisation approaches: simple (yellow), plume (orange), box (purple), PICOP (brown). The RMSE is computed following Eq.(32) in the left panel and following Eq.(33) in the right panel.

4 Discussion

4.1 Uncertainties in the tuning

The tuning of the various parameters in this study was done in a more consistent and with a larger amount of data than would be currently possible with observations, making the newly tuned parameters more representative in time and space. However, uncertainties remain, which we discuss and estimate in the following.

4.1.1 The perfect-model approach and the use of NEMO

Our perfect-model approach relies on the assumption that NEMO results in a realistic approximation of the circulation in the ice-shelf cavity and melt behaviour at the ice-ocean interface. While it is clear that NEMO does not replicate reality exactly, a part of the melt biases found in NEMO (see Appendix B) are a result of problems unrelated to the representation of the ice-shelf cavities (e.g. Southern Ocean biases related to the atmospheric forcing, the representation of sea ice, or unresolved or poorly parameterised ocean processes). Such biases do not alter the physical consistency of the relationship between ocean properties in front of ice shelves and basal melting, and are therefore not a problem for our perfect-model approach.

It is nonetheless obvious that the representation of ice-ocean exchange in NEMO is far from perfect. As presented in Sec. 2.1.1, the melt still relies on a parameterisation, which is, however, more advanced than the ones we assess. The resolution of NEMO is of several kilometers, which might hinder an accurate representation of the small-scale geometry and the small-scale processes occurring near the grounding line. As we assess the parameterisations based on NEMO's topography here, which does not include the thinnest part of the cavity near the grounding line (NEMO needs at least two vertical cells), this does not affect our conclusions whether a given parameterisation emulates well NEMO but might be a limitation of our assessment concerning applications on smaller scales.

To gain a first-order insight into the importance of the resolution in the assessment and application of the different parameterisations, we conduct a quick experiment focused on the Pine Island Glacier ice shelf, for which multiannual observational estimates of input temperature and salinity (Dutrieux et al., 2014), high-resolution topography (500 m resolution, Morlighem, 2020; Morlighem et al., 2020) and high-resolution observational estimates of the basal melt rates (32-256 m resolution, Shean et al., 2019) are available. We find that most of the parameterisations clearly underestimate the melt rates (Fig. 8b), which does not necessarily come as a surprise as it is was already visible at lower resolution (Fig. 6) and therefore rather is a result of the circum-Antarctic tuning than of the resolution. Taking into account the local slope, on the contrary, leads to a large overestimation over large parts of the ice shelf. We suggest that this is a result of small-scale irregularities in the draft geometry becoming more visible, and less smoothed out, which results in higher local slopes and higher melt rates. The overestimation implies that the local slope is not necessarily a good feature to locally adjust the melt rate.

Normalising the melt by dividing by the 90th percentile (Fig. 8c) provides an additional perspective on the pattern, more independent from biases induced by the tuning. We see that taking a constant Antarctic slope and the modified version of the plume parameterisation result in patterns closest to the observational estimates (Fig. 8a), while the normalised melt is more
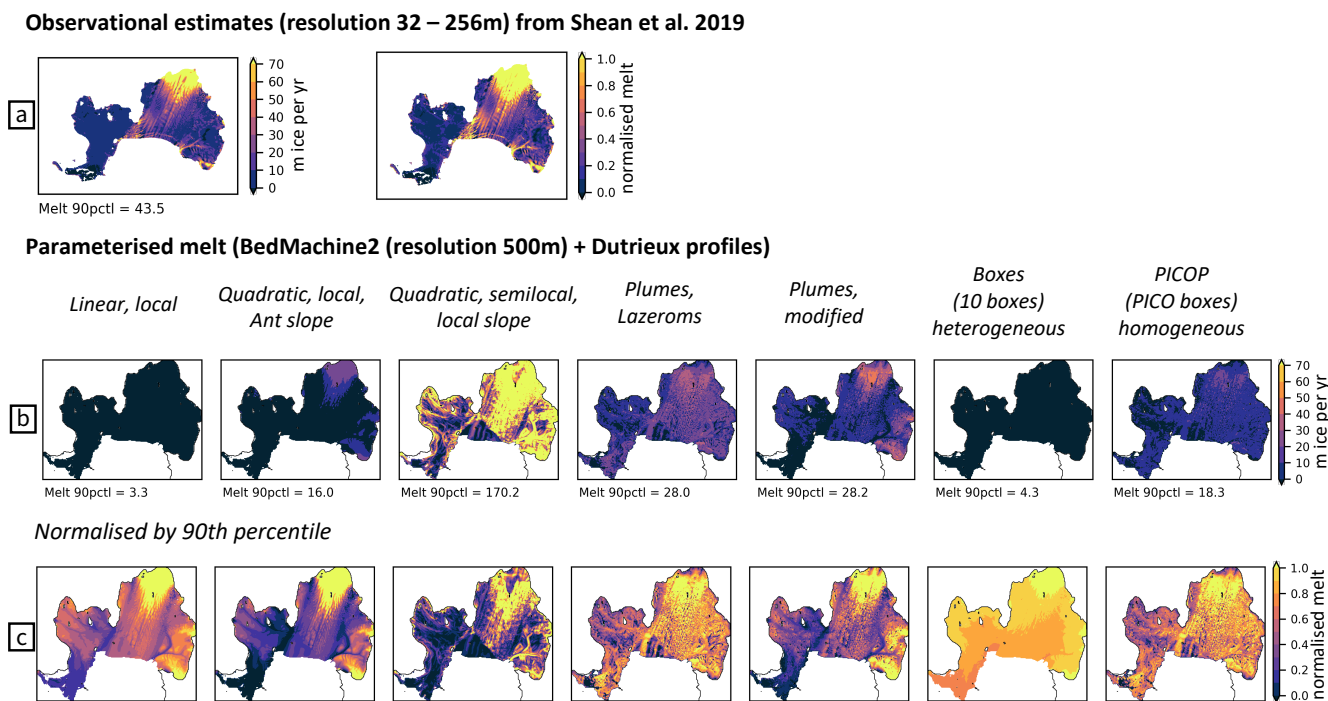
Figure 8. Comparison between (a) observational estimates inferred from remote sensing and (b) parameterised melt rates inferred based on observational estimates of input properties and topography and the tuned parameters for the Pine Island Glacier ice shelf. (c) Parameterised melt rates normalised by dividing by the 90th percentile. The observational estimates of basal melt rates (mean over 2008-2015) were inferred by Shean et al. (2019) using satellite and airborne altimetry with an "initial-pixel method" (see Fig. 7b in Shean et al., 2019). The input temperature and salinity are from Dutrieux et al. (2014) and cover 6 years (1994, 2000, 2007, 2009, 2010, 2012). The Bedmachine Antarctica version 2 dataset (Morlighem, 2020; Morlighem et al., 2020) is used for the geometric information. We averaged the parameterised basal melt patterns over the 6 years.

homogeneously distributed in the other parameterisations. This result, based on one single ice shelf, implies that the modified plume might adapt better to increasing resolution.

Nevertheless, this quick check remains focused on one ice shelf and might not provide robust conclusions applicable on the circum-Antarctic scale. Further work with alternative models (e.g. sigma-coordinate models and higher resolution) is needed to assess the uncertainty related to the use of our 1/4° NEMO simulations.

Additionally, NEMO is advantageous to use for this study as it resolves the ice-shelf cavities. However, it is run in an uncoupled mode, which means that basal melt does not affect the ice-shelf geometry. While this is unrealistic at first glance, the aim of this study was to assess the physical link between the hydrographic properties in front of the ice shelf and the melt rates. A change in geometry of the ice shelf would affect the melt patterns as such but should in principle not affect the physical link between hydrographic properties and the melt.

As we have seen with the Fimbul ice shelf, the use of yearly average input temperature and salinity does not allow the representation of seasonal melt. However, going to shorter time scales would probably require to account for the possible time lag between the input forcing entering the cavity and the occurrence of the melt (Holland, 2017), which has been ignored in
570 this study. Even with the yearly data used in our study, not accounting for the lag is a limitation for the largest ice-shelf cavities in which the residence time of water reaches several years (Michel et al., 1979; Nicholls and Østerhus, 2004).

4.1.2 Simple parameterisations

To examine the uncertainty in the tuned parameters for the simple parameterisations, we conduct a range of bootstrapping experiments. We replicate our tuning procedure by applying a least-squares linear fit, with the method presented in Sec. 2.4,
575 to 15,000 different samples chosen via bootstrapping. Each sample has the same amount of data points (36 x 127) and is composed of 36 random sub-samples, with replacement, of the different ice shelves.

The 5th, 10th, 33rd, 50th, 66th, 90th, and 95th percentiles describing the resulting distribution of 15,000 parameters for the simple parameterisations are shown in Table 11. The spread in the parameters varies depending on the parameterisation. To better grasp how the uncertainty in parameters translates into uncertainty in the resulting melt, we apply this range of
580 parameters to the "original" sample (the 36 ice shelves). The resulting spread in the RMSE of the integrated melt is small for the well-performing simple parameterisations, such as the quadratic formulations using a constant Antarctic slope or the local slope (Fig. 10, box-whisker plots), showing low uncertainty in the tuned parameter. However, the spread in the RMSE of the melt rate near the grounding line is substantially larger when using a local or cavity slope compared to a constant Antarctic slope.

Table 11. Percentiles describing the uncertainty range of the $\gamma_{TS,\text{loc, Ant}}$ for the linear local parameterisation and K for the other simple parameterisations after 15,000 bootstrap experiments with replacement. For the Antarctic slope parameterisations, K is inferred assuming that the mean local slope is $\sin\theta_{\text{Ant}} = 2.9 \times 10^{-3}$.

Parameterisation	5th	10th	33rd	Median	66th	90th	95th
Linear-local ($\times 10^{-6}$)	2.0	2.0	2.3	2.5	2.9	6.0	8.0
Quadratic-local Ant slope ($\times 10^{-5}$)	9.5	9.8	11.2	12.1	13.1	15.3	15.9
Quadratic-local cavity slope ($\times 10^{-5}$)	4.1	4.6	5.9	6.6	7.4	8.8	9.3
Quadratic-local local slope ($\times 10^{-5}$)	7.1	7.5	8.5	8.9	9.3	9.8	10.0
Quadratic-semilocal Ant slope ($\times 10^{-5}$)	10.7	11.1	12.4	13.3	14.2	16.0	16.4
Quadratic-semilocal cavity slope ($\times 10^{-5}$)	3.6	4.1	5.5	6.4	7.2	8.9	9.4
Quadratic-semilocal local slope ($\times 10^{-5}$)	7.3	7.8	8.8	9.2	9.6	10.2	10.4

585 ### 4.1.3 Complex parameterisations

As the tuning algorithms are computationally more expensive for the complex parameterisations, we cannot run 15,000 bootstrapping experiments and cannot investigate the uncertainty for each variation of the complex parameterisations. Instead, we

concentrate on a subset of parameterisations. For the Lazeroms version of the plume parameterisation, we apply the tuning
to 500 sub-samples of the ice shelves. Again, each sample has the same amount of data points (36 x 127) and is composed
590 of 36 random sub-samples, with replacement, of the different ice shelves. We also conduct 100 such experiments for the box
parameterisation with PICO homogeneous boxes, PICO heterogeneous boxes, and 10 heterogeneous boxes, respectively, as
well as for the two PICOP configurations presented earlier. The resulting parameters are shown in Fig. 9.

For the plume parameterisation, the entrainment coefficient E_0 is mainly clustered between 2 and 10×10^{-2} (Fig. 9, left).
The Stanton number $C_d^{1/2}\Gamma_{TS}$ varies between 1 and 10×10^{-4}. For low Stanton numbers, E_0 can reach very high values ($\approx 8\%$
595 of the values above 40×10^{-2}, not shown). This means that turbulent exchange and entrainment compensate each other to result
in the appropriate heat needed to match the reference melting. In contrast, there seems to be a lower threshold for the Stanton
number where very high entrainment coefficients are needed to provide the heat needed for the melting. An inverse quadratic
function can be empirically fitted to describe the relationship between the two parameters. The resulting relationship (Fig. 9a,
grey line) is:

$$600 \quad E_0 = \left[\frac{16.8}{(C_d^{1/2}\Gamma_{TS} \times 10^4)^2} + 2.2 \right] \times 10^{-2} \tag{34}$$

If only fitted to the main cluster (for $E_0 < 15$, Fig. 9a, black line), the fit results in the following relationship:

$$E_0 = \left[\frac{7.2}{(C_d^{1/2}\Gamma_{TS} \times 10^4)^2} + 3.8 \right] \times 10^{-2} \tag{35}$$

Table 12. Percentiles describing the uncertainty range of the $\gamma_T^\star$ for the box parameterisation and $C_d^{1/2}\Gamma_{TS}$ for the plume and PICOP
parameterisation for the other simple parameterisations after several bootstrap experiments with replacement as shown in Fig. 9.

Parameterisation	5th	10th	33rd	Median	66th	90th	95th
Plume, Lazeroms $C_d^{1/2}\Gamma_{TS} \times 10^{-4}$, 500 bootstrap samples)	1.3	1.4	1.7	1.9	2.1	2.7	3.0
Boxes, PICO boxes ($\gamma_T^\star \times 10^{-5}$, 200 bootstrap samples)	0.21	0.24	0.37	0.45	0.57	1.54	1.96
Boxes, 10-box setup ($\gamma_T^\star \times 10^{-5}$, 100 bootstrap samples)	0.24	0.29	0.46	0.59	0.80	1.61	2.27
PICOP, 10-box setup ($C_d^{1/2}\Gamma_{TS} \times 10^{-4}$, 100 bootstrap samples)	0.96	1.0	1.5	2.7	7.2	7.8×10^2	1.7×10^5
PICOP, PICO boxes ($C_d^{1/2}\Gamma_{TS} \times 10^{-4}$, 100 bootstrap samples)	0.95	1.1	2.1	4.9	7.3	9.1×10^4	12×10^4

For the box parameterisation, the distribution of parameters resulting from the bootstrap experiments also hints to an inverse
quadratic relationship between the overturning coefficient C and the effective turbulent temperature exchange velocity $\gamma_T^\star$,
605 which seems consistent across the three different configurations presented here (Fig. 9b). The lower the former, the higher the
latter, and the other way. The empirical fit resulting from this distribution is:

$$C = \left[\frac{3.3}{(\gamma_T^\star \times 10^5)^2} - 0.9 \right] \times 10^6 \tag{36}$$

One explanation for this behaviour is that, if the overturning coefficient is high, water masses are rapidly replaced and new
heat to melt the ice is supplied more often. In that case, not as much turbulent heat exchange is needed at the ice-ocean interface
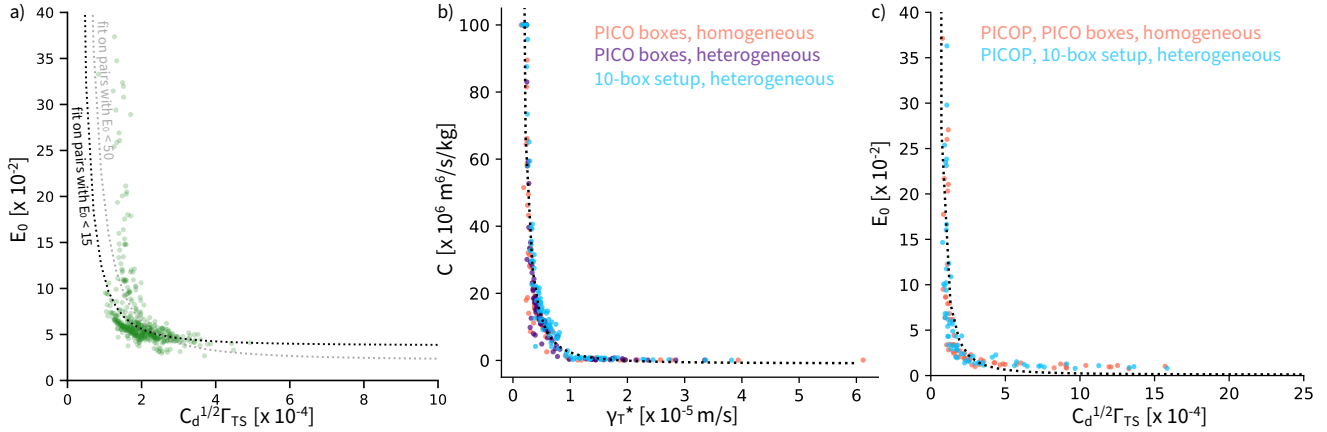
Figure 9. Distribution of the parameters resulting from the bootstrap experiments applied to the subset of complex parameterisations. (a) Distribution of $C_d^{1/2}\Gamma_{TS}$ and E_0 in 500 tuning experiments for the Lazeroms version of the plume parameterisation. (b) Distribution of C and $\gamma_T^\star$ in 100 tuning experiments for 3 different configurations, respectively. (c) Distribution of $C_d^{1/2}\Gamma_{TS}$ and E_0 in 100 tuning experiments for 2 different PICOP configurations, respectively. An inverse quadratic function has been fit empirically for the different pairs of parameters. Note that we cut the axes for better visibility. For the plumes, 8% of the E_0 are larger than 40×10^{-2}. For the boxes, C was constrained to values below 100×10^6 during tuning. For PICOP, 18% of the E_0 are larger than 40×10^{-2} and 19% of the $C_d^{1/2}\Gamma_{TS}$ are larger than 25×10^{-4}.

610 to match the reference melting. Conversely, if C is small, turbulent exchange has to be more efficient to extract enough heat from less rapidly changing water masses to lead to a similar melting.

For the PICOP parameterisation, there is also a clear relationship between $C_d^{1/2}\Gamma_{TS}$ and E_0, which reflects a similar compensating behaviour as seen in the box and plume parameters (Fig. 9c). In this case, it is best described by an inverse quadratic fit of the form:

$$615 \quad E_0 = \left[\frac{13.6}{(C_d^{1/2}\Gamma_{TS} \times 10^4)^2} + 0.1 \right] \times 10^{-2} \tag{37}$$

This relationship is different to Eq. (34) and Eq. (35), although these are supposed to be the same parameters. This highlights that these parameters potentially encompass different processes in the plume or in the PICOP parameterisation. Note that some of the higher values of $C_d^{1/2}\Gamma_{TS}$ and E_0 are several orders of magnitude higher than expected (see e.g. Table 12), which we cannot explain.

620 The empirical relationships provided in Equations (34) to (37) may be used in the future to tune complex parameterisations based on a single parameter. They can also be used to sample uncertainty, e.g. for a large ensemble, based on only one of the two parameters. We provide the uncertainty distribution resulting from our bootstrap experiments for $\gamma_T^\star$ and $C_d^{1/2}\Gamma_{TS}$ in Table 12. Note, however, that these distributions might not be as robust as the distributions for the parameters of the simple parameterisations (as shown in Table 11) due to the much smaller sample size.

Using the range of parameters as input to the box parameterisation leads to a spread in the RMSE by around 10 Gt/yr between the 25th and 75th percentile in the integrated melt but a comparatively small spread for the melt near the grounding line (Fig. 10). On the opposite, the distribution of parameters for the PICOP parameterisation does not lead to a large spread on the shelf level but a high spread for the melt near the grounding line. For the plume parameterisation, the spread in the RMSE for the integrated melt is comparable to the spread for the quadratic parameterisations with constant Antarctic slope, except large outliers on the upper end.
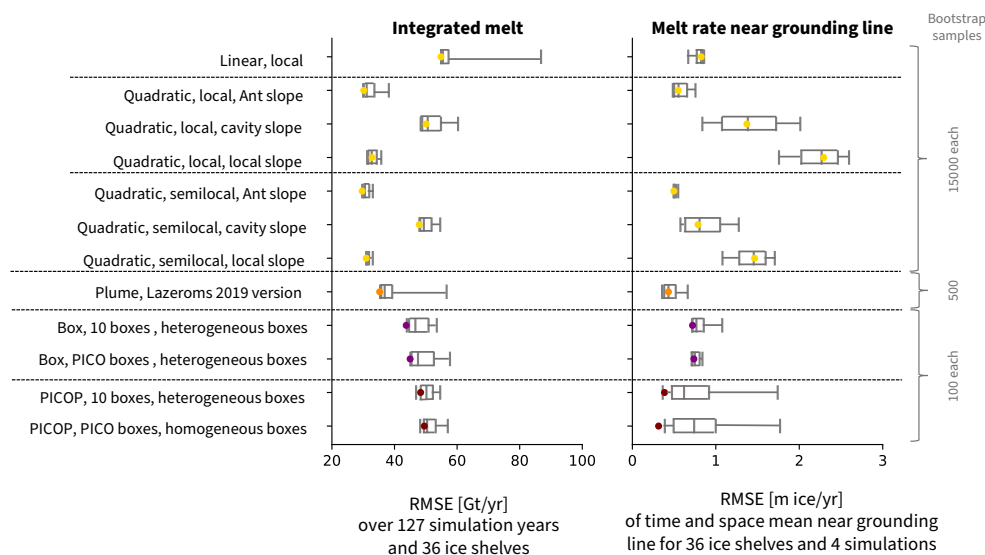
Figure 10. Left: Summary of the RMSE of the integrated melt over the 36 individual ice shelves and 127 simulation years [in Gt/yr]. The box-whisker plots show the distribution of the RMSE when using the parameters resulting from the bootstrap experiments (shown in Table 11 and Fig. 9). Right: Same but for the RMSE of the melt averaged over time and space near the grounding line (average in the first box of the 5-box-setup) over the 36 individual ice shelves and four simulations [in m ice/yr]. The colors represent the different parameterisation approaches: simple (yellow), plume (orange), box (purple), PICOP (brown). The RMSE is computed following Eq.(32) in the left panel and following Eq.(33) in the right panel. The box-whisker plots indicate the 10th, 25th, 50th, 75th and 90th percentile.

4.2 Recommendations and limitations

This study has pointed out different behaviours, and strengths and weaknesses for the different parameterisations. In the following, we discuss emerging recommendations and limitations for the use of the basal melt parameterisations in ice-sheet models.

4.2.1 Simple parameterisations

The simple parameterisations are most practical to implement in ice-sheet or ocean models. The good performance of the quadratic formulations is therefore a positive signal for further ice-sheet model development. Especially, we could show that the newly tuned parameters result in similar RMSE to the parameters given as recommendations for ISMIP6 simulations for the "MeanAnt" case (see Jourdain et al., 2020). This means that basal melt rates in the standard ISMIP6 experiments are reasonably consistent with our 1/4° global ocean simulations.

In contrast, the ISMIP6 parameters for the "PIGL" case and the parameters proposed by Favier et al. (2019) lead to high RMSE in our case, and therefore can only be used in combination with appropriate temperature corrections. Here we have decided not to use corrections as temperatures are perfectly known in our approach, but the PIGL corrections certainly partly have a physical origin (heat consumed by melt), which is not accounted for in our simple parameterisations.

We also found only modest improvements from the semilocal compared to the local parameterisations, which may be considered as a good reason to use the local version which is easier to implement. To our surprise, the inclusion of the slope gave poorer comparisons to NEMO at the scale of Antarctica, with a tendency to produce too strong melt rates near grounding lines. The slope-dependent parameterisation is nonetheless relatively good for cavity melt rates and could be used as end members in ensemble simulations to include members with high melt rates near grounding lines.

Finally, the linear-local parameterisation yields the highest RMSE of all parameterisations and should therefore be replaced by a quadratic formulation in further ice-sheet model developments.

In regard to spatial patterns, the simple parameterisations do not exhibit any refreezing, while the box parameterisation has large areas of refreezing. Currently, the ice shelves are largely melting so areas of refreezing might not be of interest for projections. However, further work is needed to characterise how important these regions are and, if they are crucial, how to better represent them in the different parameterisations.

4.2.2 Plume parameterisation

The results for the plume parameterisation are very satisfying both for the integrated melt and the melt near the grounding line and suggest that it is a good approximation of the processes at work below the ice shelf. The modification, which takes into account more precisely the effect of upstream properties, does not lead to clear improvement in the RMSE. At the same time, the quick check in Sec. 4.1.1 suggests that the modification adapts better to an increase in resolution. We therefore suggest to, when possible, try out both versions of the plume parameterisation presented here to increase our understanding of how they compare in different applications and which one to prefer in which context.

4.2.3 Box parameterisation

The box parameterisation is implemented as PICO in several ice-sheet models, most prominently in the Parallel Ice Sheet Model PISM (Winkelmann et al., 2011). Our study provides us with new insights into its limitations and potential improvements.

We find that the amount of boxes slightly influences the tuning of $\gamma_T^\star$ and C while there is nearly no difference between the tuned parameters using homogeneous or heterogeneous boxes. A higher amount of boxes leads to a slightly lower RMSE. If the box parameterisation is used, we therefore recommend using a setup similar to the 10-box setup for all ice shelves. Nonetheless, this also means that if an implementation of the PICO boxes already exists in the ice-sheet model of interest, it is 670 probably not worth changing that setup, if the corresponding newly tuned parameters are used.

While it mimics some of the physical processes at work (essentially advection and heat conservation), the RMSE associated with the box parameterisation is high compared to the quadratic non-slope dependent and plume parameterisations. It is similar or better than the "cavity slope" option, and similar or better than the local slope for melt near the grounding line, in general better than the linear parameterisation. The box parameterisation performs best for the offshore input compared to the other 675 parameterisations. In general, the box parameterisation seems to be robust in its results, and shows no large variations when testing the number of boxes, the homogeneous or heterogeneous approach, different ocean input regions and the parameter selection sensitivity.

We suggest that one limitation of the box parameterisation is using the ocean bottom temperature as input temperature. To investigate this, we apply the input temperatures used for the box parameterisation (ocean bottom temperatures) as input for the 680 simple parameterisations. We then re-tune the simple parameterisations. The resulting RMSE using these re-tuned parameters for the simple parameterisations is about 10 Gt/yr higher than the RMSE shown in Sec. 3.1.1. This is an indication that the bottom temperature is not necessarily an appropriate input temperature. Further in that direction, we also ran a tuning of the box parameterisation using the depth of the grounding line when it is shallower than the average entrance depth. In this case, the effect was a reduction in the RMSE by about 3 to 4 Gt/yr. One possible improvement for the future development is therefore 685 possibly defining other criteria for the input temperatures.

Another limitation could be that the box parameterisation assumes a linear relationship between the thermal forcing and the melt, like in the linear-local parameterisation, which was shown to not adequately represent the melt (see e.g. Fig. 7). Our results suggest that incorporating a quadratic relationship in the further development of the box parameterisation might improve it significantly.

690 **4.2.4 PICOP parameterisation**

Our results do not encourage the use of PICOP as a melt parameterisation. It represents well the melt near the grounding line, but does not perform well for the integrated melt in our analyses. Also our uncertainty quantification shows that the distribution of parameters can lead to a large variation in the performance (see e.g. Fig. 10). As it is based on PICO and the plume parameterisation, any improvement in any of the two might improve PICOP's performance. Additionally, the way in 695 which both are combined might be improved as well.

4.2.5 Definition of input temperature and salinity

Our results clearly indicate that averaging temperatures and salinity on the continental shelf and close to the ice shelf front (50 km domain) give the best results in comparison to averaging offshore properties. This should be the way to derive tem-

peratures from the CMIP models. For coarser ocean models, like those used in climate models of intermediate complexity,
700   the parameter values tuned for offshore temperatures might be preferred as these models are too coarse to represent the conti-
nental shelf around most of Antarctica. A better approach for these very coarse models may be to complement the basal melt
parameterisation with a sub-grid description of on-shelf processes.

Here, the parameter values have been tuned for yearly temperatures and salinity, and we therefore recommend to keep this
consistency. We have nonetheless shown that this fails to capture "mode 3" melt (Jacobs et al., 1992; Dinniman et al., 2016)
705   related to the seasonal variability for some ice shelves like the Fimbul ice shelf. So further work will be needed to evaluate other
input frequencies, although this may require to retune the parameters and probably to estimate the lags between temperature
and basal melt variations (see Holland, 2017).

Biases can also be introduced by using one averaged profile for a whole ice shelf, especially for large ice shelves, under which
complex circulation patterns can be found. However, as each ice shelf has a specific circulation pattern, it is not straightforward
710   to define more precise regions of interest for the input properties that are applicable to all ice shelves. Further research in
that direction could identify more delimited domains of inflow and strengthen the link between input properties and melt, and
therefore reduce uncertainties in the use of parameterisations. At the same time, such regions might change in a changing
climate. So, this identification should adapt to changing conditions.

4.2.6   Other comments

715   All parameterisations investigated here heavily rely on a horizontally homogenous vertical circulation within the ice-shelf cav-
ity. While the plume parameterisation and quadratic formulation take into account some extent the horizontal component of the
circulation of the water masses in their formulation of U, additional factors such as the asymmetry of the circulation related to
the Coriolis force, tides, or irregularities in the sub-shelf bathymetry can also affect the thermal forcing at the ice-ocean inter-
face. At the same time, as every ice-shelf cavity has a different geometry such effects are challenging to parameterise in general
720   formulations. Further work is needed to overcome these challenges and include these effects into the melt parameterisations.

Also, our results and conclusions hold for circum-Antarctic applications, such as large-scale Antarctic ice-sheet simulations.
We do not claim that the parameterisations performing best on the circum-Antarctic scale are also performing best for each
individual ice shelf. For regional studies, some parameterisations might perform better if tuned only for the region of interest.
However, this would mean that the given parameterisation is not adapted to generalisation and therefore potentially prone to
725   biases in changing conditions.

We also do not claim to have covered every possible melt sensitivity to input ocean properties. We use an ensemble of
simulations to introduce variations in the input forcing (up to 2 K for some cavities) and therefore include the melt sensitivity
to the input ocean temperatures in our tuning. Nevertheless, in some of the cavities, such as the ice shelves in the Weddell sector,
the variations between the different simulations remain very small. The melt sensitivity to larger variations in all regions could
730   be explored more in future work.

5   Summary & conclusions

In a perfect-model approach, we re-tune the most commonly used basal melt parameterisations and assess their performance in representing the melt at the base of Antarctic ice shelves, on a circum-Antarctic scale. We also provide an uncertainty range for the tuned parameters.

735   We conclude that:

- Better performances are found when using input hydrographic profiles averaged over a domain of 50 km on the continental shelf in front of the ice shelf compared to averaged over an offshore domain, beyond the continental shelf.

- The tuned simple quadratic local and semilocal parameterisations using a constant Antarctic slope (i.e. no slope dependency), and the plume parameterisation yield the best compromise to represent well both integrated shelf melt and melt near the grounding line.

740

- If input is only available for the offshore domain, the box parameterisation and the quadratic parameterisation using one cavity slope per ice shelf yield the comparatively best results but with clearly lower accuracy than when using the better-performing parameterisations with 50 km input.

None of the parameterisations yields a negligible RMSE compared to the reference, with RMSEs on the same order as or
745 even larger than the reference value. Parameterising basal melt therefore still remains a challenge. However, we are confident that ongoing development will further reduce uncertainties in the representation of basal melt in ice-sheet models. Especially, the growing amount of high-resolution ocean simulations becoming available through the Ice Shelf Ocean MIP (ISOMIP) and Marine Ice Sheet-Ocean MIP (MISOMIP) projects provides large amounts of data as a testbed to advance our understanding of basal melt and further refine basal melt parameterisations.

750 **Appendix A: More details about the NEMO configuration**

The horizontal (vertical) advection of tracers is done using respectively a fourth order (second order) Flux Corrected Transport scheme based on Zalesak (1979). A free slip lateral boundary condition on momentum is applied with no slip condition applied locally at Bering strait, Gibraltar and along the West Greenland coast. A quadratic bottom and top (ocean/ice shelf interface) friction is used with an increased bottom friction in the Indonesian Throughflow, Denmark Strait and Bab-el-Mandel. The
755 bottom (top) drag is set respectively at 1×10^{-3} (2.5×10^{-3}).

A polynomial approximation of the TEOS10 equation of state is used (Roquet et al., 2015). Internal wave mixing is parameterised following de Lavergne et al. (2016). Finally, in some simulations, a 3D temperature and salinity restoring of the Antarctic Bottom Water (AABW) is applied based on the method presented by Dufour et al. (2012). The data used for the AABW restoring are from Gouretski and Koltermann (2004). Other model setup choices as momentum advection, lateral dif-
760 fusion of momentum and tracer, vertical mixing (TKE), convection, double diffusion, bottom boundary layer are as described in Storkey et al. (2018).

The sea ice model used here is SI3 which is based on LIM 3.6 (Rousset et al., 2015). Five ice thickness categories are used to represent the sub-grid-scale ice thickness distribution. Halo-thermodynamics are represented with two ice layers and one snow layer. The ice dynamic is based on the modified elastic-viscous-plastic (EVP) rheology (Bouillon et al., 2013) or an adaptative EVP rheology (Kimmritz et al., 2016).

Freshwater fluxes and heat fluxes are represented as follows. A sea surface salinity restoring is applied toward 1980-2010 WOA2018 surface climatological salinity (Zweng et al., 2018) in order to avoid large drifts in the salinity and overturning circulation. The strength of the restoring is set to -166.666 mm day^{-1} psu^{-1} (piston velocity of about 60m/yr). In order to preserve coastal runoff, the restoring coefficient is fading toward the coast (length scale of 150 km as described in Dussin et al. (2012)). River runoff comes from the Dai and Trenberth (2002) climatology.

All the various settings are widely used parameters if not, reasonable choices. The isopycnal diffusion of 150 m^2/s (300 m^2/s) has been used respectively in Storkey et al. (2018) (Megann et al., 2014). AABW restoring has been used with success in Dufour et al. (2012). The use of an eddy induced velocity to parameterise eddy diffusivity in a 0.25° resolution simulation is debated. Storkey et al. (2018) in their global 0.25° resolution configuration do not use an eddy parameterisation but not in their next version (Storkey et al., pers. comm.). In a MITgcm simulation at similar resolution, Naughten et al. (2019) used such a parameterisation. Change in the sea ice parameters has been done to increase Antarctic sea-ice production and indirectly HSSW production via brine rejection.

Appendix B: More details about the ensemble of simulations

Here, we present some key indicators to assess the quality of the REALISTIC simulation in the vicinity of Antarctica. The ACC transport at Drake passage is about 125 Sv over the last twenty years of the simulation (Fig. B1c). It compares reasonably well with the estimates of 136.7±7.8 Sv derived from CTD and ADCP data (Cunningham et al., 2003). This low transport is mainly explained by the too light AABW on the shelf break. A restoring experiment (Dufour et al., 2012, , and WARMROSS) clearly shows that artificially maintaining the AABW decreases the spin-up time of the ACC and drives a stronger ACC at a level within the observation range. The strength of the two main gyres (Weddell Gyre and Ross Gyre) represented in the REALISTIC simulations is in agreement with previous NEMO simulations at similar resolution (Mathiot et al., 2011). The REALISTIC Weddell gyre strength (Fig. B1a) is however on the high side of observation-based estimates to 56±8 Sv (Klatt et al., 2005). REALISTIC Ross Gyre strength (Fig. B1b) is also on the high side compared to the 20±5 Sv SOSE estimates (Mazloff et al., 2010).

The REALISTIC simulation is able to reproduce a cold Ross and Weddell shelf and warm Bellingshausen and Amundsen Seas comparable to the WOA2018 observation (Fig. B2). The associated basal melt for Ross Ice Shelf (RIS), Filchner Ronne Ice shelf (FRIS), Pine Island Glacier (PIG) and all Antarctic ice shelves is reasonably well represented comparing to observational (Rignot et al., 2013) estimates (Fig. B1d,e,f,g). With a low melt and even weak freezing in the interior, the REALISTIC RIS basal melt pattern compares well against Rignot et al. (2013) estimates. We notice, however, too much melting on the East and West sides along the ice shelf front. The FRIS basal melt pattern is also well represented with respect to Rignot et al.
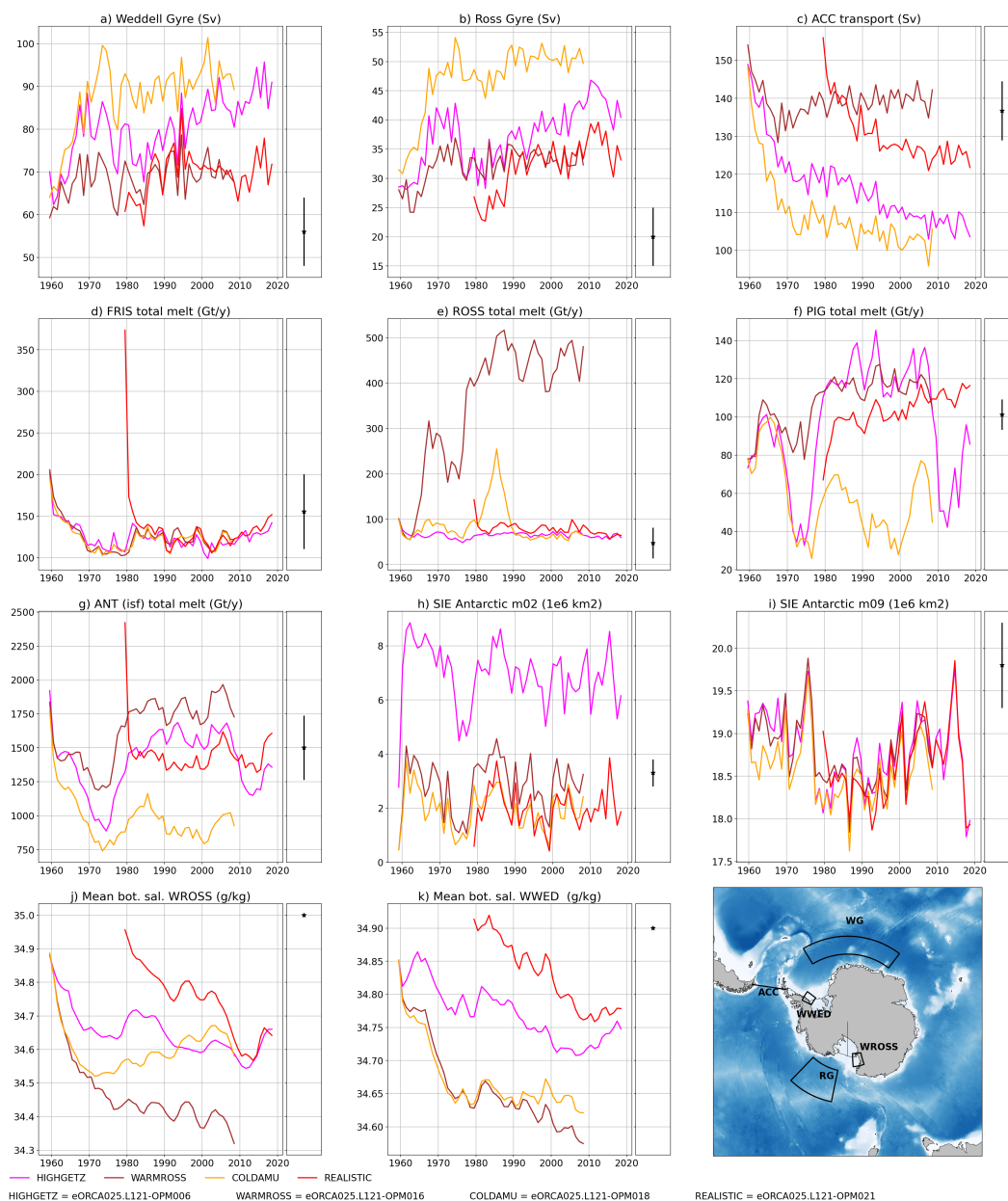
Figure B1. Time evolution of Weddell gyre strength (a), Ross gyre strength (b), ACC transport through Drake passage (c), FRIS, RIS, PIG and Antarctica total basal melt (respectively d, e, f and g) and Antarctic sea ice extent in February (h) and (i). In black: the observation estimates respectively from Klatt et al. (2005), Mazloff et al. (2010), Cunningham et al. (2003), Rignot et al. (2013) (d, e, f, g) and Meier et al. (2017) (h, i) and WOA2018 (1981-2010) by Zweng et al. (2018) (j,k). Panel (l) is a map showing the boxes used to compute the mean bottom salinity (j,k), gyre strength (a,b) and the Drake passage section used in (c).
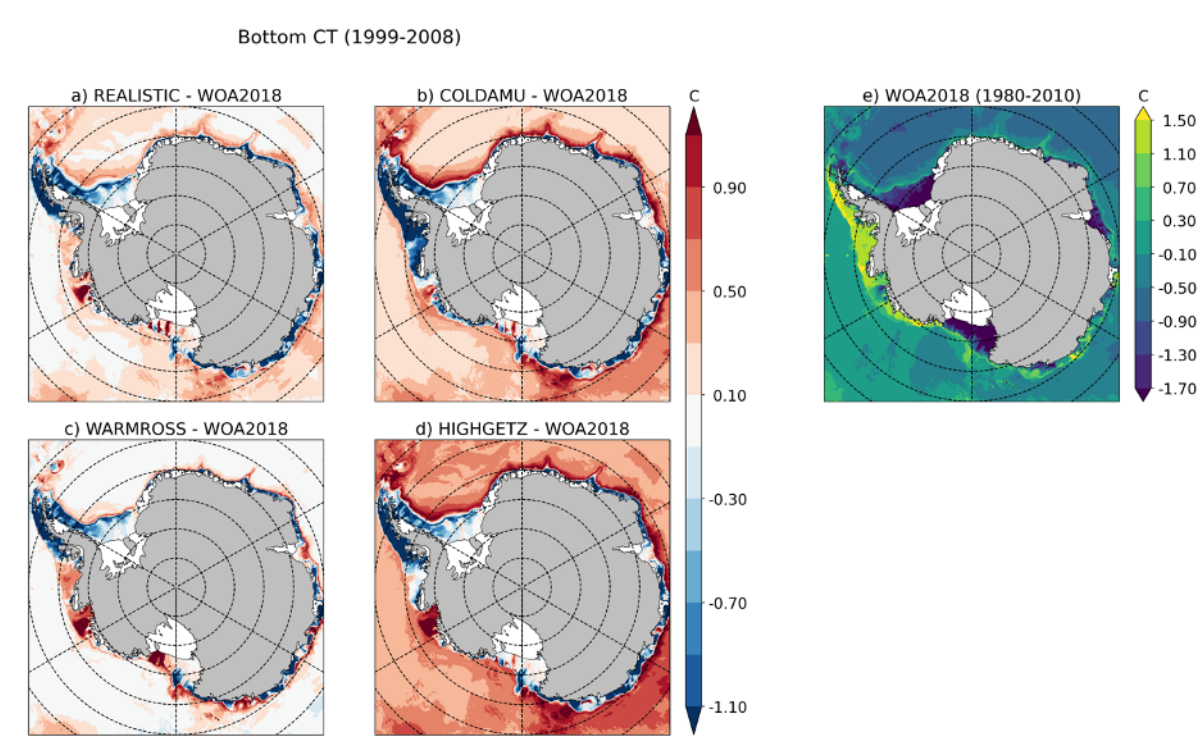
Figure B2. (a-d) Bottom temperature averaged over the period 1999-2008 compared to WOA2018 bottom temperature (1981-2010) [model - observation]. (e) Bottom temperature in WOA2018 (1981-2010).

795 (2013) estimates with freezing in the vicinity of the various rumples in the interior and along the East side of Berkner Island and stronger melting along the grounding line in the deepest part of the cavity and along the ice shelf front. For the PIG, it has been shown that the melt is driven by buoyancy plumes concentrated within the 20 km of the grounding line (Dutrieux et al., 2013) into 1 km scale channels. The buoyancy plume dynamics are not well represented in NEMO due to its z coordinates and the resolution needed to represent the channels is well beyond the resolution of most global ocean configuration. So, not

800 surprisingly, we cannot expect to have realistic melt pattern close to the grounding lines. REALISTIC HSSW properties at the formation sites on Ross and Weddell continental shelf are slightly too fresh compared with WOA2018 (Fig. B1j,k) but salty enough to keep both RIS and FRIS driven by HSSW inflow (call mode 1 in Jacobs et al. (1992)). Similar HSSW has been modelised in Mathiot et al. (2017) at similar horizontal resolution with an ERA-Interim based atmospheric forcing. This is a known bias in NEMO simulations forced by reanalysis re-enforced by the fact West Antarctic Ice Shelf basal melt is on the

805 high end compared to the observations (example with PIG in Fig. B1f). The REALISTIC Antarctic summer and winter sea-ice extents (Fig. B1h,i) are rather well represented compared to the satellite estimates Meier et al. (2017).

The Amundsen sea bottom temperature varies from a too cold state in COLDAMU to a too warm state (WARMROSS). WARMROSS also triggers a warm state over East Ross shelf and much fresher high salinity shelf water (HSSW). These

changes in the shelf temperature lead to large variability in basal melt of the Ross ice shelf and Pine Island Glacier (Fig. B1e,

810   f). In WARMROSS, the basal melt of the Eastern part of the Ross ice shelf is driven by warm modified circumpolar deep water

(MCDW) intrusions and fresher HSSW compared to the REALISTIC run. In COLDAMU, the cooling of the Amundsen and

Bellingshausen Sea triggers a collapse in the basal melting of the ice shelves. The large variability between the simulations is

also visible in the Antarctic integrated melt (Fig. B1g).

Appendix C: Amount of boxes in the different box model configurations

Table C1. Amount of boxes in the three different box model setups. When the amount is smaller than the name of the setup, it means that the amount of boxes needed to be reduced to have an ascendant slope or that the ice shelf is too small for this amount of boxes.

Ice shelf	2 boxes setup	5 boxes setup	10 boxes setup	PICO setup
Filchner	2	5	10	4
Ronne	2	5	10	5
Venable	1	2	3	2
George VI	1	1	2	3
Abbot	2	5	8	3
Stange	2	4	5	3
Larsen C	2	4	5	3
Bach	1	2	3	2
Larsen D	2	3	4	3
Wilkins	1	2	3	3
Getz (REALISTIC, COLDAMU, WARMROSS)	2	4	5	3
Getz (HIGHGETZ)	2	3	4	3
Thwaites	1	2	3	2
Crosson	2	5	8	3
Dotson	2	5	6	2
Cosgrove	1	1	2	2
Pine Island	2	5	6	2
Ross	2	5	10	5
Cook	1	2	3	2
Nickerson	2	4	5	2
Sulzberger	2	5	6	2
Amery	2	5	10	3
Moscow University	1	2	3	2
Tracy Tremenchus	1	1	2	2
Totten	2	5	9	2
West	2	4	5	3
Shackleton	2	5	10	3
Ekstrom	2	5	10	2
Nivl	2	5	7	3
Prince Harald	2	3	4	2
Riiser-Larsen	2	5	7	3
Fimbul	2	5	10	4
Roi Baudoin	2	5	8	3
Lazarev	2	5	9	3
Stancomb Brunt	2	5	10	4
Jelbart	2	5	7	3
Borchgrevink	2	5	9	3

Appendix D: Heatmaps

815
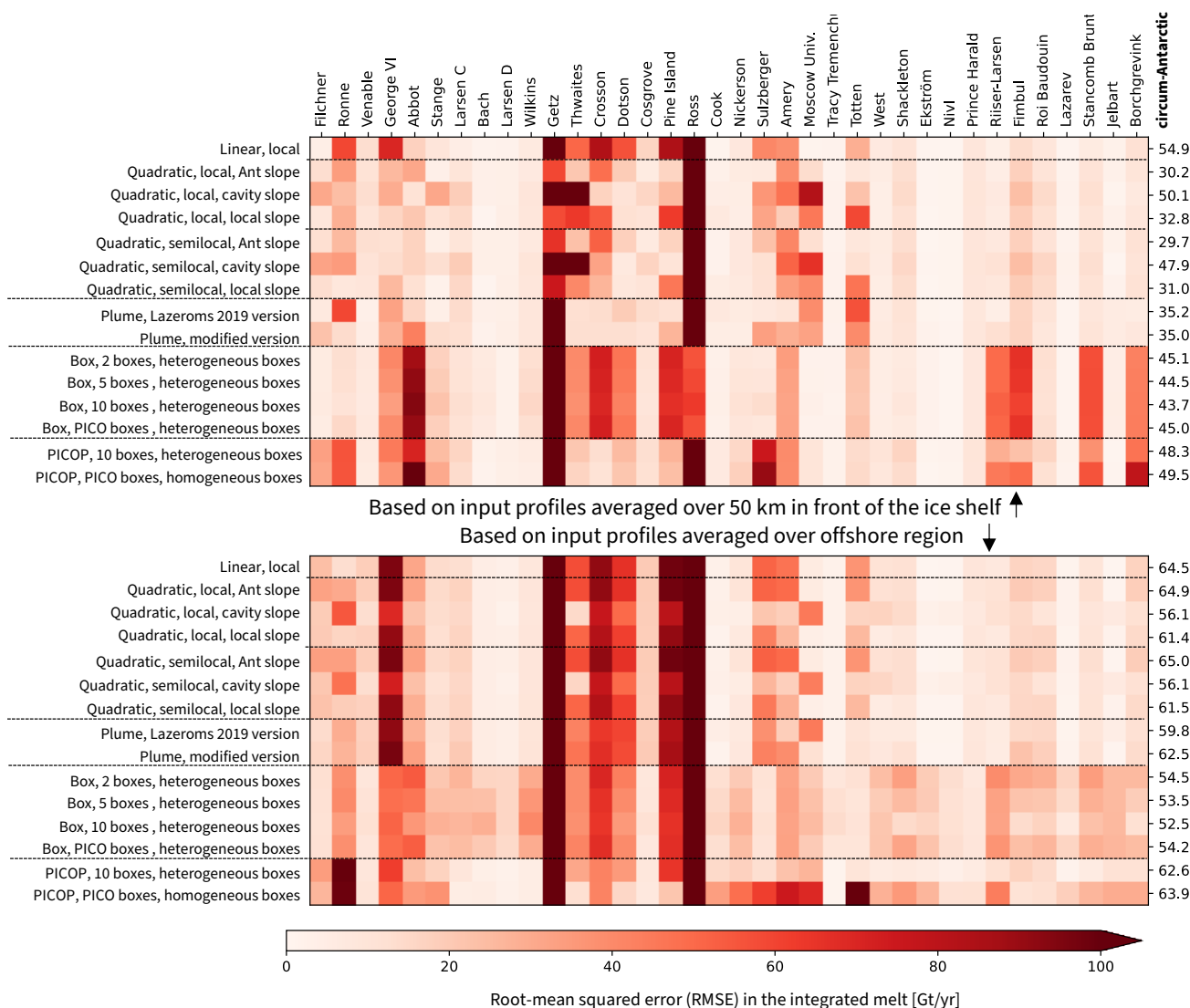
Figure D1. RMSE between parameterised and reference integrated ice-shelf melt with the tuned parameters. The RMSE of individual ice shelves are diagnosed from yearly averages across all four simulations (127 years in total). The values on the right are the RMSE calculated across the 127 years of simulation and across all 36 individual ice shelves. Results are shown for the 50 km (upper panel) and the offshore (lower panel) domains.
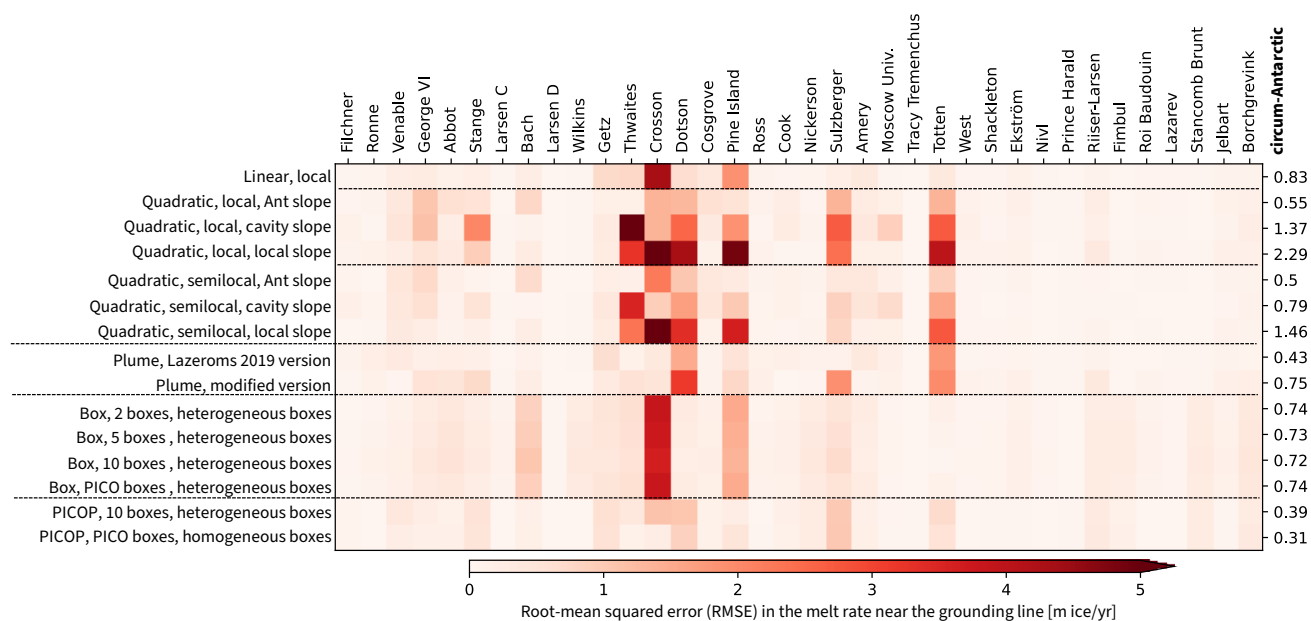
Figure D2. RMSE between parameterised and reference melt averaged over time and space near the grounding line. The RMSE of individual ice shelves are diagnosed from the time-mean averaged spatially over approximately the 10% of the ice shelf nearest to the grounding line (area covered by the first box in the 5 boxes configuration of the box parameterisation) across the four simulations. The values on the right are the RMSE calculated across the 36 ice shelves and the four simulations.

Code and data availability. The NEMO simulation output is documented on https://github.com/pmathiot/NEMOCFG and the data will be uploaded on zenodo. All code used to handle the simulation output and produce the figures, as well as the package containing the parameterisations will be available on https://github.com/ClimateClara and uploaded on zenodo as well upon acceptance of this manuscript.

Author contributions. CB and NCJ developed the original idea of this paper. CB carried out all analyses and wrote most of the manuscript.
820 PM carried out the simulations and wrote the manuscript parts relating to the NEMO configuration and difference between the simulations. AJ suggested the "modified" formulation of the plume parameterisation. CB, NCJ, RR, AJ, and PM contributed to discussions.

Competing interests. The authors declare that they have no conflict of interest.

Acknowledgements. We thank David E. Shean for sharing his observational estimates of the basal melt rates with us. Most of the computations presented in this paper were performed using the GRICAD infrastructure (https://gricad.univ-grenoble-alpes.fr), which is supported
825 by Grenoble research communities. The NEMO simulations were performed using HPC resources from GENCI–CINES (MISOCS project, allocations A0080106035 and A0100106035). This publication was supported by PROTECT. This project has received funding from the European Union's Horizon 2020 research and innovation programme under grant agreement No 869304, PROTECT contribution number XX.

References

830   Adcroft, A. and Campin, J.: Rescaled height coordinates for accurate representation of free-surface flows in ocean circulation models, Ocean Modelling, 7, 269–284, https://doi.org/10.1016/j.ocemod.2003.09.003, 2004.

Adusumilli, S., Fricker, H., Medley, B., Padman, L., and Siegfried, M.: Interannual variations in meltwater input to the Southern Ocean from Antarctic ice shelves, Nature Geoscience, 13, 616–620, https://doi.org/10.1038/s41561-020-0616-z, 2020.

Álvarez-Solas, J., Montoya, M., Ritz, C., Ramstein, G., Charbit, S., Dumas, C., Nisancioglu, K., Dokken, T., and Ganopolski, A.: Heinrich

835   event 1: an example of dynamical ice-sheet reaction to oceanic changes, Climate of the Past, 7, 1297–1306, https://doi.org/10.5194/cp-7-1297-2011, 2011.

Amante, C. and Eakins, B.: ETOPO1 Global Relief Model converted to PanMap layer format, https://doi.org/10.1594/PANGAEA.769615, nOAA-National Geophysical Data Center, 2009.

Arzeno, I., Beardsley, R., Limeburner, R., Owens, B., Padman, L., Springer, S., Stewart, C., and Williams, M.: Ocean variability con-

840   tributing to basal melt rate near the ice front of Ross Ice Shelf, Antarctica, Journal of Geophysical Research: Oceans, 119, 4214–4233, https://doi.org/10.1002/2014JC009792, 2014.

Asay-Davis, X., Cornford, S., Durand, G., Galton-Fenzi, B., Gladstone, R., Gudmundsson, G., Hattermann, T., Holland, D., Holland, D., Holland, P., Martin, D., Mathiot, P., Pattyn, F., and Seroussi, H.: Experimental design for three interrelated marine ice sheet and ocean model intercomparison projects: MISMIP v. 3 (MISMIP +), ISOMIP v. 2 (ISOMIP +) and MISOMIP v. 1 (MISOMIP1), Geosci. Model

845   Dev., 9, 2471–2497, https://doi.org/10.5194/gmd-9-2471-2016, 2016.

Asay-Davis, X., Jourdain, N., and Nakayama, Y.: Developments in Simulating and Parameterizing Interactions Between the Southern Ocean and the Antarctic Ice Sheet, Current Climate Change Reports, 3, 316–329, https://doi.org/10.1007/s40641-017-0071-0, 2017.

Barthel, A., Agosta, C., Little, C., Hattermann, T., Jourdain, N., Goelzer, H., Nowicki, S., Seroussi, H., Straneo, F., and Bracegirdle, T.: CMIP5 model selection for ISMIP6 ice sheet model forcing: Greenland and Antarctica, The Cryosphere, 14, 2020.

850   Beadling, R., Russell, J., Stouffer, R., Mazloff, M., Talley, L., Goodman, P., Sallée, J., Hewitt, H., Hyder, P., and Pandde, A.: Representation of Southern Ocean Properties across Coupled Model Intercomparison Project Generations: CMIP3 to CMIP6, Journal of Climate, 33, 6555–6581, https://doi.org/10.1175/JCLI-D-19-0970.1, 2020.

Beckmann, A. and Goosse, H.: A parameterization of ice shelf–ocean interaction for climate models, Ocean Modelling, 5, 157–170, https://doi.org/10.1016/S1463-5003(02)00019-7, 2003.

855   Bett, D., Holland, P., Naveira Garabato, A., Jenkins, A., Dutrieux, P., Kimura, S., and Fleming, A.: The Impact of the Amundsen Sea Freshwater Balance on Ocean Melting of the West Antarctic Ice Sheet, Journal of Geophysical Research: Oceans, 125, https://doi.org/10.1029/2020JC016305, 2020.

Bouillon, S., Fichefet, T., Legat, V., and Madec, G.: The elastic–viscous–plastic method revisited, Ocean Modelling, 71, 2–12, https://doi.org/10.1016/j.ocemod.2013.05.013, 2013.

860   Branch, M., Coleman, T., and Li, Y.: A Subspace, Interior, and Conjugate Gradient Method for Large-Scale Bound-Constrained Minimization Problems, SIAM Journal on Scientific Computing, 21, 1–23, https://doi.org/10.1137/S1064827595289108, 1999.

Bull, C., Jenkins, A., Jourdain, N., Vaňková, I., Holland, P., Mathiot, P., Hausmann, U., and Sallée, J.: Remote Control of Filchner-Ronne Ice Shelf Melt Rates by the Antarctic Slope Current, Journal of Geophysical Research: Oceans, 126, https://doi.org/10.1029/2020JC016550, 2021.

865   Burgard, C.: Multimelt, a python framework to apply existing basal melt parameterisation, https://github.com/ClimateClara/multimelt, 2021.

Cunningham, S., Alderson, S., and Kin, B.: Transport and variability of the Antarctic Circumpolar Current in Drake Passage, Journal of Geophysical Research, 108, 8084, https://doi.org/10.1029/2001JC001147, 2003.

Dai, A. and Trenberth, K. E.: Estimates of Freshwater Discharge from Continents: Latitudinal and Seasonal Variations, Journal of Hydrometeorology, 3, 660–687, https://doi.org/10.1175/1525-7541(2002)003<0660:EOFDFC>2.0.CO;2, 2002.

870 Dask Development Team: Dask: Library for dynamic task scheduling, https://dask.org, 2016.

de Lavergne, C., Madec, G., Le Sommer, J., Nurser, A., and Naveira Garabato, A.: The Impact of a Variable Mixing Efficiency on the Abyssal Overturning, Journal of Physical Oceanography, 46, 663–681, https://doi.org/10.1175/JPO-D-14-0259.1, 2016.

De Rydt, J. and Gudmundsson, G.: Coupled ice shelf-ocean modeling and complex grounding line retreat from a seabed ridge, Journal of Geophysical Research: Earth Surface, 121, 865–880, https://doi.org/10.1002/2015JF003791, 2016.

875 De Rydt, J., Holland, P., Dutrieux, P., and Jenkins, A.: Geometric and oceanographic controls on melting beneath Pine Island Glacier, Journal of Geophysical Research: Oceans, 119, 2420–2438, 2014.

DeConto, R. and Pollard, D.: Contribution of Antarctica to past and future sea-level rise, Nature, 531, 591–597, https://doi.org/10.1038/nature17145, 2016.

Dinniman, M., Asay-Davis, X., Galton-Fenzi, B., Holland, P., Jenkins, A., and Timmermann, R.: Modeling Ice Shelf/Ocean Interaction in
880 Antarctica: A Review, Oceanography, 29, 144–153, https://doi.org/10.5670/oceanog.2016.106, 2016.

Dufour, C., Le Sommer, J., Zika, J., Gehlen, M., Orr, J., Mathiot, P., and Barnier, B.: Standing and transient eddies in the response of the Southern Ocean meridional overturning to the Southern annular mode, Journal of Climate, 25, https://doi.org/10.1175/JCLI-D-11-00309.1, 2012.

Dussin, R., Molines, J., and Barnier, B.: Definition of the interannual experiment ORCA025.L75-GRD100, 1958-2010, 2012.

885 Dutrieux, P., Vaughan, D., Corr, H., Jenkins, A., Holland, P., Joughin, I., and Fleming, A.: Pine Island glacier ice shelf melt distributed at kilometre scales, The Cryosphere, 7, 1543–1555, https://doi.org/10.1175/JCLI-D-19-0203.1, 2013.

Dutrieux, P., De Rydt, J., Jenkins, A., Holland, P., Ha, H., Lee, S., Steig, E., Ding, Q., Abrahamsen, E., and Schröder, M.: Strong Sensitivity of Pine Island Ice-Shelf Melting to Climatic Variability, Science, 343, 174–178, https://doi.org/10.1126/science.1244341, 2014.

Edwards, T. and the ISMIP6 Team: Projected land ice contributions to twenty-first-century sea level rise, Nature, 593, 74–82,
890 https://doi.org/10.1038/s41586-021-03302-y, 2021.

Eyring, V., Bony, S., Meehl, G., Senior, C., Stevens, B., Stouffer, R., and Taylor, K.: Overview of the Coupled Model Intercomparison Project Phase 6 (CMIP6) experimental design and organization, Geosci. Model Dev., 9, 1937–1958, https://doi.org/10.5194/gmd-9-1937-2016, 2016.

Favier, L., Jourdain, N., Jenkins, A., Merino, N., Durand, G., Gagliardini, O., Gillet-Chaulet, F., and Mathiot, P.: Assessment of sub-shelf
895 melting parameterisations using the ocean–ice-sheet coupled model NEMO(v3.6)–Elmer/Ice(v8.3), Geoscientific Model Development, 12, 2255–2283, https://doi.org/10.5194/gmd-12-2255-2019, 2019.

Gagliardini, O., Durand, G., Zwinger, T., Hindmarsh, R., and Le Meur, E.: Coupling of ice-shelf melting and buttressing is a key process in ice-sheets dynamics, Geophysical Research Letters, 37, 2010.

Garcia, H., Boyer, T., Baranova, O., Locarnini, R., Mishonov, A., Grodsky, A., Paver, C., Weathers, K., Smolyar, I., Reagan, J., Seidov, D.,
900 and Zweng, M.: World Ocean Atlas 2018: Product Documentation., 2019.

Gent, P. and McWilliams, J.: Isopycnal Mixing in Ocean Circulation Models, Journal of Physical Oceanography, 20, 150–155, https://doi.org/10.1175/1520-0485(1990)020<0150:IMIOCM>2.0.CO;2, 1990.

Gouretski, V. and Koltermann, K.: WOCE Global Hydrographic Climatology, A Technical Report, 2004.

Goutorbe, B., Poort, J., Lucazeau, F., and Raillard, S.: Global heat flow trends resolved from multiple geological and geophysical proxies, Geophysical Journal International, 187, 1405–1419, https://doi.org/10.1111/j.1365-246X.2011.05228.x, 2011.

Gudmundsson, G., Krug, J., Durand, G., Favier, L., and Gagliardini, O.: The stability of grounding lines on retrograde slopes, The Cryosphere, 6, 1497–1505, https://doi.org/10.5194/tc-6-1497-2012, 2012.

Harris, C., Millman, K., van der Walt, S., Gommers, R., Virtanen, P., Cournapeau, D., Wieser, E., Taylor, J., Berg, S., Smith, N., Kern, R., Picus, M., Hoyer, S., van Kerkwijk, M., Brett, M., Haldane, A., del Río, J., Wiebe, M., Peterson, P., Gérard-Marchant, P., Sheppard, K., Reddy, T., Weckesser, W., Abbasi, H., Gohlke, C., and Oliphant, T.: Array programming with NumPy, Nature, 585, 357–362, https://doi.org/10.1038/s41586-020-2649-2, 2020.

Hausmann, U., Sallée, J., Jourdain, N., Mathiot, P., Rousset, C., Madec, G., Deshayes, J., and Hattermann, T.: The Role of Tides in Ocean-Ice Shelf Interactions in the Southwestern Weddell Sea, Journal of Geophysical Research: Oceans, https://doi.org/10.1029/2019JC015847, 2020.

Heuzé, C.: Antarctic Bottom Water and North Atlantic Deep Water in CMIP6 models, Ocean Science, 17, 59–90, https://doi.org/10.5194/os-17-59-2021, 2021.

Hill, E. A., Rosier, S. H. R., Gudmundsson, G. H., and Collins, M.: Quantifying the potential future contribution to global mean sea level from the Filchner-Ronne basin, Antarctica, The Cryosphere Discussions, 2021, 1–43, https://doi.org/10.5194/tc-2021-120, 2021.

Hoffman, M., Asay-Davis, X., Price, S., Fyke, J., and Perego, M.: Effect of Subshelf Melt Variability on Sea Level Rise Contribution From Thwaites Glacier, Antarctica, Journal of Geophysical Research: Earth Surface, 124, 2798–2822, https://doi.org/10.1029/2019JF005155, 2019.

Holland, P., Jenkins, A., and Holland, D.: The Response of Ice Shelf Basal Melting to Variations in Ocean Temperature, Journal of Climate, 21, 2558–2572, https://doi.org/10.1175/2007JCLI1909.1, 2008.

Holland, P. R.: The transient response of ice shelf melting to ocean change, Journal of Physical Oceanography, 47, 2101–2114, https://doi.org/10.1175/JPO-D-17-0071.1, 2017.

Howard, S. L., Padman, L., and Erofeeva, S.: CATS2008: Circum-Antarctic Tidal Simulation version 2008, https://doi.org/10.15784/601235, 2019.

Hoyer, S. and Hamman, J.: xarray: N-D labeled arrays and datasets in Python, Journal of Open Research Software, 5, https://doi.org/10.5334/jors.148, 2017.

Huot, P.-V., Fichefet, T., Jourdain, N., Mathiot, P., Rousset, C., Kittel, C., and Fettweis, X.: Influence of ocean tides and ice shelves on ocean–ice interactions and dense shelf water formation in the D'Urville Sea, Antarctica, Ocean Modelling, 162, 101 794, https://doi.org/10.1016/j.ocemod.2021.101794, 2021.

IHO and BODC IOC: Centenary Edition of the GEBCO Digital Atlas, published on CD-ROM on behalf of the Intergovernmental Oceanographic Commission and the International Hydrographic Organization as part of the General Bathymetric Chart of the Oceans; British Oceanographic Dat, organization as part of the General Bathymetric Chart of the Oceans, British Oceanographic Data Centre, Liverpool, UK, 2003.

Jacobs, S., Helmer, H., Doake, C., Jenkins, A., and Frolich, R.: Melting of ice shelves and the mass balance of Antarctica, Journal of Glaciology, 38, https://doi.org/10.1017/S0022143000002252, 1992.

Jacobs, S., Jenkins, A., Giulivi, C., and Dutrieux, P.: Stronger ocean circulation and increased melting under Pine Island Glacier ice shelf, Nature Geoscience, 4, 519–523, https://doi.org/10.1038/ngeo1188, 2011.

Jenkins, A.: A one-dimensional model of ice shelf-ocean interaction, Journal of Geophysical Research: Oceans, 96, 20 671–20 677, https://doi.org/10.1029/91JC01842, 1991.

Jenkins, A., Nicholls, K., and Corr, H.: Observation and Parameterization of Ablation at the Base of Ronne Ice Shelf, Antarctica, Journal of Physical Oceanography, 40, 2298–2311, https://doi.org/10.1175/2010JPO4317.1, 2010.

945   Jenkins, A., Shoosmith, D., Dutrieux, P., Jacobs, S., Kim, T., Lee, S., Ha, H. K., and Stammerjohn, S.: West Antarctic Ice Sheet retreat in the Amundsen Sea driven by decadal oceanic variability, Nature Geoscience, 11, 733–738, https://doi.org/10.1038/s41561-018-0207-4, 2018.

Joughin, I., Shapero, D., Dutrieux, P., and Smith, B.: Ocean-induced melt volume directly paces ice loss from Pine Island Glacier, Science Advances, 7, https://doi.org/10.1126/sciadv.abi5738, 2021.

Jourdain, N., Mathiot, P., Merino, N., Durand, G., Le Sommer, J., Dutrieux, P., Spence, P., and Madec, G.: Ocean circulation and sea-ice
950   thinning induced by melting ice shelves in the Amundsen Sea, J. Geophys. Res., 122, 2550–2573, https://doi.org/10.1002/2016JC012509, 2017.

Jourdain, N., Molines, J.-M., Le Sommer, J., Mathiot, P., Chanut, J., de Lavergne, C., and Madec, G.: Simulating or prescribing the influence of tides on the Amundsen Sea ice shelves, Ocean Modelling, 133, 44–55, https://doi.org/10.1016/j.ocemod.2018.11.001, 2019.

Jourdain, N., Asay-Davis, X., Hattermann, T., Straneo, F., Seroussi, H., Little, C., and Nowicki, S.: A protocol for calculating basal melt
955   rates in the ISMIP6 Antarctic ice sheet projections, The Cryosphere, 14, 3111–3134, https://doi.org/10.5194/tc-14-3111-2020, 2020.

Kageyama, M., Braconnot, P., Harrison, S., Haywood, A., Jungclaus, J., Otto-Bliesner, B., Peterschmitt, J.-Y., Abe-Ouchi, A., Albani, S., Bartlein, P., Brierley, C., Crucifix, M., Dolan, A., Fernandez-Donado, L., Fischer, H., Hopcroft, P., Ivanovic, R., Lambert, F., Lunt, D., Mahowald, N., Peltier, W., Phipps, S., Roche, D., Schmidt, G., Tarasov, L., Valdes, P., Zhang, Q., and Zhou, T.: The PMIP4 contribution to CMIP6 – Part 1: Overview and over-arching analysis plan, Geoscientific Model Development, 11, 1033–1057,
960   https://doi.org/10.5194/gmd-11-1033-2018, 2018.

Khazendar, A., Rignot, E., Schroeder, D., Seroussi, H., Schodlok, M., Scheuchl, B.and Mouginot, J., Sutterley, T., and Velicogna, I.: Rapid submarine ice melting in the grounding zones of ice shelves in West Antarctica, Nature Communications, 7, 13 243, https://doi.org/10.1038/ncomms13243, 2016.

Kimmritz, M., Danilov, S., and Losch, M.: The adaptive EVP method for solving the sea ice momentum equation, Ocean Modelling, 101,
965   59–67, https://doi.org/10.1016/j.ocemod.2016.03.004, 2016.

Klatt, O., Fahrbach, E., Hoppema, M., and Rohardt, G.: The transport of the Weddell Gyre across the Prime Meridian, Deep-Sea Research Part II: Topical Studies in Oceanography, 52, 513–528, https://doi.org/10.1016/j.dsr2.2004.12.015, 2005.

Kraft, D. A.: A software package for sequential quadratic programming., tech. Rep. DFVLR-FB 88-28, DLR German Aerospace Center – Institute for Flight Mechanics, Koln, Germany., 1988.

970   Kreuzer, M., Reese, R., Huiskamp, W., Petri, S., Albrecht, T., Feulner, G., and Winkelmann, R.: Coupling framework (1.0) for the PISM (1.1. 4) ice sheet model and the MOM5 (5.1. 0) ocean model via the PICO ice shelf cavity model in an Antarctic domain, Geoscientific Model Development, 14, 3697–3714, https://doi.org/10.5194/gmd-14-3697-2021, 2021.

Large, W. and Yeager, S.: The global climatology of an interannually varying air–sea flux data set, Climate Dynamics, 33, 341–364, https://doi.org/10.1007/s00382-008-0441-3, 2009.

975   Lazeroms, W., Jenkins, A., Gudmunsson, G., and van de Wal, R.: Modelling present-day basal melt rates for Antarctic ice shelves using a parametrization of buoyant meltwater plumes, The Cryosphere, 12, 49–70, https://doi.org/10.5194/tc-12-49-2018, 2018.

Lazeroms, W., Jenkins, A., Rienstra, S., and van de Wal, R.: An Analytical Derivation of Ice-Shelf Basal Melt Based on the Dynamics of Meltwater Plumes, Journal of Physical Oceanography, 49, 917–939, https://doi.org/10.1175/JPO-D-18-0131.1, 2019.

Lipscomb, W., Leguy, G., Jourdain, N., Asay-Davis, X., Seroussi, H., and Nowicki, S.: ISMIP6-based projections of ocean-forced Antarctic
980   Ice Sheet evolution using the Community Ice Sheet Model, The Cryosphere, 15, 633–661, https://doi.org/10.5194/tc-15-633-2021, 2021.

Little, C., Gnanadesikan, A., and Oppenheimer, M.: How ice shelf morphology controls basal melting, Journal of Geophysical Research:
       Oceans, 114, https://doi.org/10.1029/2008JC005197, 2009.

Locarnini, R., Mishonov, A., Baranova, O., Boyer, T., Zweng, M., Garcia, H., Reagan, J., Seidov, D., Weathers, K., Paver, C., and Smolyar,
       I.: World Ocean Atlas 2018, Volume 1: Temperature., 2018.

985   Marsh, R., Ivchenko, V., Skliris, N., Alderson, S., Bigg, G., Madec, G., Blaker, A., Aksenov, Y., Sinha, B., Coward, A., Le Sommer, J.,
       Merino, N., and Zalesny, V.: NEMO–ICB (v1.0): interactive icebergs in the NEMO ocean model globally configured at eddy-permitting
       resolution, Geosci. Model Dev., 8, 1547–1562, https://doi.org/10.5194/gmd-8-1547-2015, 2015.

Martin, M., Winkelmann, R., Haseloff, M., Albrecht, T., Bueler, E., Khroulev, C., and Levermann, A.: The potsdam parallel
       ice sheet model (PISM-PIK)–Part 2: dynamic equilibrium simulation of the antarctic ice sheet, The Cryosphere, 5, 727–740,
990   https://doi.org/10.1002/2013JC009513, 2011.

Mathiot, P., Goosse, H., Fichefet, T., Barnier, B., and Gallée, H.: Modelling the seasonal variability of the Antarctic Slope Current, Ocean
       Science, 7, 455–470, https://doi.org/10.5194/os-7-455-2011, 2011.

Mathiot, P., Jenkins, A., Harris, C., and Madec, G.: Explicit representation and parametrised impacts of under ice shelf seas in the $z^{\star}$
       coordinate ocean model NEMO 3.6, Geoscientific Model Development, 10, 2849–2874, https://doi.org/10.5194/gmd-10-2849-2017, 2017.

995   Mazloff, M., Heimbach, P., and Wunsch, C.: An eddy-permitting Southern Ocean state estimate, Journal of Physical Oceanography, 40,
       880–899, https://doi.org/10.1175/2009JPO4236.1, 2010.

Megann, A., Storkey, D., Aksenov, Y., Alderson, S., Calvert, D., Graham, T., Hyder, P., Siddorn, J., and Sinha, B.: GO5.0:
       the joint NERC–Met Office NEMO global ocean model for use in coupled and forced applications, Geoscie. Model Dev., 7,
       https://doi.org/10.5194/gmd-7-1069-2014, 2014.

1000 Meier, W., Fetterer, F., Savoie, M., Mallory, S., Duerr, R., and Stroeve, J.: NOAA/NSIDC Climate Data Record of Passive Microwave Sea
       Ice Concentration, Version 3, https://nsidc.org/data/g02202/versions/3, 2017.

Merino, N., Le Sommer, J., Durand, G., Jourdain, N., Madec, G., Mathiot, P., and Tournadre, J.: Antarctic icebergs melt over the Southern
       Ocean: Climatology and impact on sea ice, Ocean Modelling, 104, 99–110, https://doi.org/10.1016/j.ocemod.2016.05.001, 2016.

Michel, R., Linick, T., and Williams, P.: Tritium and carbon-14 distributions in seawater from under the Ross Ice Shelf Project ice hole,
1005   Science, 203, 445–446, 1979.

Morlighem, M.: MEaSUREs BedMachine Antarctica, Version 2., https://doi.org/10.5067/E1QL9HFQ7A8M, boulder, Colorado USA. NASA
       National Snow and Ice Data Center Distributed Active Archive Center., 2020.

Morlighem, M., Rignot, E., Binder, T., Blankenship, D., Drews, R., Eagles, G., Eisen, O., Ferraccioli, F., Forsberg, R., Fretwell, P., Goel, V.,
       Greenbaum, J., Gudmundsson, H., Guo, J., Helm, V., Hofstede, C., Howat, I., Humbert, A., Jokat, W., Karlsson, N., Lee, W., Matsuoka,
1010   K., Millan, R., Mouginot, J., Paden, J., Pattyn, F., Roberts, J., Rosier, S., Ruppel, A., Seroussi, H., Smith, E., Steinhage, D., Sun, B.,
       van den Broeke, M., van Ommen, T., van Wessem, M., and Young, D.: Deep glacial troughs and stabilizing ridges unveiled beneath the
       margins of the Antarctic ice sheet, Nature Geoscience, 13, 132–137, https://doi.org/10.1038/s41561-019-0510-8, 2020.

Morlighem, M., Goldberg, D., Dias dos Santos, T., Lee, J., and Sagebaum, M.: Mapping the Sensitivity of the Amund-
       sen Sea Embayment to Changes in External Forcings Using Automatic Differentiation, Geophysical Research Letters, 48,
1015   https://doi.org/10.1029/2021GL095440, 2021.

Mouginot, J., Rignot, E., and Scheuchl, B.: Sustained increase in ice discharge from the Amundsen Sea Embayment, West Antarctica, from 1973 to 2013, Geophysical Research Letters, 41, 1576–1584, https://doi.org/10.1002/2013GL059069, 2014.

Nakayama, Y., Timmermann, R., Schröder, M., and Hellmer, H. H.: On the difficulty of modeling Circumpolar Deep Water intrusions onto the Amundsen Sea continental shelf, Ocean Modelling, 84, 26–34, https://doi.org/10.1016/j.ocemod.2014.09.007, 2014.

Naughten, K., Jenkins, A., Holland, P., Mugford, R., Nicholls, K., and Munday, D.: Modeling the Influence of the Weddell Polynya on the Filchner–Ronne Ice Shelf Cavity, Journal of Climate, 32, https://doi.org/10.1175/JCLI-D-19-0203.1, 2019.

NEMO Sea Ice Working Group: Sea Ice modelling Integrated Initiative (SI3) — The NEMO sea ice engine, Scientific Notes of Climate Modelling Center, 31, https://doi.org/10.5281/zenodo.1471689, iSSN 1288-1619, Institut Pierre-Simon Laplace, 2019.

NEMO Team: NEMO ocean engine, Scientific Notes of Climate Modelling Center, 27, https://doi.org/10.5281/zenodo.1464816, 2019.

Nicholls, K. W. and Østerhus, S.: Interannual variability and ventilation timescales in the ocean cavity beneath Filchner-Ronne Ice Shelf, Antarctica, Journal of Geophysical Research: Oceans, 109, 2004.

Nowicki, S., Goelzer, H., Seroussi, H., Payne, A., Lipscomb, W., Abe-Ouchi, A., Agosta, C., Alexander, P., Asay-Davis, X., Barthel, A., et al.: Experimental protocol for sea level projections from ISMIP6 stand-alone ice sheet models, The Cryosphere, 14, 2331–2368, https://doi.org/10.5194/tc-14-2331-2020, 2020.

Olbers, D. and Hellmer, H.: A box model of circulation and melting in ice shelf caverns, Ocean Dynamics, 60, 141–153, https://doi.org/10.1007/s10236-009-0252-z, 2010.

Oppenheimer, M., Glavovic, B., Hinkel, J., van de Wal, R., Magnan, A., Abd-Elgawad, A., Cai, R., Cifuentes-Jara, M., DeConto, R., Ghosh, T., Hay, J., Isla, F., Marzeion, B., Meyssignac, B., and Sebesvari, Z.: Sea Level Rise and Implications for Low-Lying Islands, Coasts and Communities, chapter 4, Cambridge University Press, Cambridge, United Kingdom and New York, NY, USA, 2019.

Padman, L., Erofeeva, S., and Fricker, H.: Improving Antarctic tide models by assimilation of ICESat laser altimetry over ice shelves, Geophysical Research Letters, 35, L22 504, https://doi.org/10.1029/2008GL035592, 2008.

Paolo, F., Fricker, H., and Padman, L.: Volume loss from Antarctic ice shelves is accelerating, Science, 348, 327–331, https://doi.org/10.1126/science.aaa0940, 2015.

Pelle, T., Morlighem, M., and Bondzio, J.: Brief communication: PICOP, a new ocean melt parameterization under ice shelves combining PICO and a plume model, The Cryosphere, 13, 1043–1049, https://doi.org/10.5194/tc-13-1043-2019, 2019.

Reese, R., Albrecht, T., Mengel, M., Asay-Davis, X., and Winkelmann, R.: Antarctic sub-shelf melt rates via PICO, The Cryosphere, 12, 1969–1985, https://doi.org/10.5194/tc-12-1969-2018, 2018.

Reese, R., Levermann, A., Albrecht, T., Seroussi, H., and Winkelmann, R.: The role of history and strength of the oceanic forcing in sea level projections from Antarctica with the Parallel Ice Sheet Model, The Cryosphere, 14, 3097–3110, https://doi.org/10.5194/tc-14-3097-2020, 2020.

Richter, O., Gwyther, D., King, M., and Galton-Fenzi, B.: Tidal modulation of Antarctic ice shelf melting, The Cryosphere Discussions, pp. 1–32, https://doi.org/10.5194/tc-2020-169, 2020.

Rignot, E., Jacobs, S., Mouginot, J., and Scheuchl, B.: Ice-shelf melting around Antarctica, Science, 341, 266–270, https://doi.org/10.1126/science.1235798, 2013.

Rignot, E., Mouginot, J., Morlighem, M., Seroussi, H., and Scheuchl, B.: Widespread, rapid grounding line retreat of Pine Island, Thwaites, Smith, and Kohler glaciers, West Antarctica, from 1992 to 2011, Geophysical Research Letters, 41, 3502–3509, https://doi.org/10.1002/2014GL060140, 2014.

Roquet, F., Madec, G., McDougall, T., and Barker, P.: Accurate polynomial expressions for the density and specific volume of seawater using the TEOS-10 standard, Ocean Modelling, 90, 29–43, https://doi.org/10.1016/j.ocemod.2015.04.002, 2015.

1055 Rousset, C., Vancoppenolle, M., Madec, G., Fichefet, T., Flavoni, S., Barthélemy, A., Benshila, R., Chanut, J., Levy, C., and Masson, S.: The Louvain-La-Neuve sea ice model LIM3.6: global and regional capabilities, Geosci. Model Dev., 8, 2991–3005, https://doi.org/10.5194/gmd-8-2991-2015, 2015.

Scheuchl, B.and Mouginot, J., Rignot, E., Morlighem, M., and Khazendar, A.: Grounding line retreat of Pope, Smith, and Kohler Glaciers, West Antarctica, measured with Sentinel-1a radar interferometry data, Geophysical Research Letters, 43, 8572–8579,

1060 https://doi.org/10.1002/2016GL069287, 2016.

Schoof, C.: Ice sheet grounding line dynamics: Steady states, stability, and hysteresis, J. Geophys. Res., 112, F03S28, https://doi.org/10.1029/2006JF000664, 2007.

Seroussi, H., Nakayama, Y., Larour, E., Menemenlis, D., Morlighem, M., Rignot, E., and Khazendar, A.: Continued retreat of Thwaites Glacier, West Antarctica, controlled by bed topography and ocean circulation, Journal of Geophysical Research: Earth Surface, 44, 6191–

1065 6199, https://doi.org/10.1002/2017GL072910, 2017.

Shean, D., Joughin, I., Dutrieux, P., Smith, B., and Berthier, E.: Ice shelf basal melt rates from a high-resolution digital elevation model (DEM) record for Pine Island Glacier, Antarctica, The Cryosphere, 13, 2633–2656, https://doi.org/10.5194/tc-13-2633-2019, 2019.

Shen, Q., Wang, K., Shum, C., Jiang, L., Hsu, H., and Dong, J.: Recent high-resolution Antarctic ice velocity maps reveal increased mass loss in Wilkes Land, East Antarctica, Scientific Reports, 8, 4477, https://doi.org/10.1038/s41598-018-22765-0, 2018.

1070 Stern, A., Adcroft, A., and Sergienko, O.: The effects of Antarctic iceberg calving-size distribution in a global climate model, J. Geophys. Res. Oceans, 121, 5773–5788, https://doi.org/10.1002/2016JC011835, 2016.

Storkey, D., Blaker, A., Mathiot, P., Megann, A., Aksenov, Y., Blockley, E., Calvert, D., Graham, T., Hewitt, H., Hyder, P., Kuhlbrodt, T., Rae, J., and Sinha, B.: UK Global Ocean GO6 and GO7: a traceable hierarchy of model resolutions, Geoscientific Model Development, 11, 3187–3213, https://doi.org/10.5194/gmd-11-3187-2018, 2018.

1075 Taylor, K., Stouffer, R., and Meehl, G.: An Overview of CMIP5 and the Experiment Design, Bulletin of the American Meteorological Society, 93, 485–498, https://doi.org/10.1175/BAMS-D-11-00094.1, 2012.

The IMBIE Team: Mass balance of the Antarctic Ice Sheet from 1992 to 2017, Nature, 558, 219–222, https://doi.org/10.1038/s41586-018-0179-y, 2018.

Tsujino, H., Urakawa, S., Nakano, H., Small, R., Kim, W., Yeager, S., Danabasoglu, G., Suzuki, T., Bamber, J., Bentsen, M., Böning,

1080 C., Bozec, A., Chassignet, E., Curchitser, E., Boeira Dias, F., Durack, P., Griffies, S., Harada, Y., Ilicak, M., Josey, S., Kobayashi, C., Kobayashi, S., Komuro, Y., Large, W., Le Sommer, J., Marsland, S., Masina, S., Scheinert, M., Tomita, H., Valdivieso, M., and Yamazaki, D.: JRA-55 based surface dataset for driving ocean–sea-ice models (JRA55-do), Ocean Modelling, 130, 79–139, https://doi.org/10.1016/j.ocemod.2018.07.002, 2018.

Virtanen, P., Gommers, R., Oliphant, T., Haberland, M., Reddy, T., Cournapeau, D., Burovski, E., Peterson, P., Weckesser, W., Bright, J.,

1085 van der Walt, S., Brett, M., Wilson, J., Millman, K., Mayorov, N., Nelson, A., Jones, E., Kern, R., Larson, E., Carey, C., Polat, İ., Feng, Y., Moore, E., VanderPlas, J., Laxalde, D., Perktold, J., Cimrman, R., Henriksen, I., Quintero, E., Harris, C., Archibald, A., Ribeiro, A., Pedregosa, F., van Mulbregt, P., and SciPy 1.0 Contributors: SciPy 1.0: Fundamental Algorithms for Scientific Computing in Python, Nature Methods, 17, 261–272, https://doi.org/10.1038/s41592-019-0686-2, 2020.

Weertman, J.: Stability of the Junction of an Ice Sheet and an Ice Shelf, Journal of Glaciology, 13, 3–11,

1090 https://doi.org/10.3189/S0022143000023327, 1974.

Winkelmann, R., Martin, M. A., Haseloff, M., Albrecht, T., Bueler, E., Khroulev, C., and Levermann, A.: The Potsdam Parallel Ice Sheet Model (PISM-PIK) Part 1: Model description, The Cryosphere, 5, 715–726, https://doi.org/10.5194/tc-5-715-2011, 2011.

Wouters, B., Martin-Español, A., Helm, V., Flament, T., van Wessem, J., Ligtenberg, S., van den Broeke, M., and Bamber, J.: Dynamic thinning of glaciers on the Southern Antarctic Peninsula, Science, 348, 899–903, https://doi.org/10.1126/science.aaa5727, 2015.

1095 Zalesak, S.: Fully multidimensional flux-corrected transport algorithms for fluids, Journal of Computational Physics, 31, https://doi.org/10.1016/0021-9991(79)90051-2, 1979.

Zweng, M., Reagan, J., Seidov, D., Boyer, T., Locarnini, R., Garcia, H., Mishonov, A., Baranova, O., Weathers, K., Paver, C., and Smolyar, I.: World Ocean Atlas 2018, Volume 2: Salinity., 2018.